Shedding Light on the Stability and Structure–Property Relationships of Two-Dimensional Hybrid Lead Bromide Perovskites

Eugenia Vasileiadou, Ido Hadar, Mikael Kepenekian, Jacky Even, Qing Tu,
Christos Malliakas, Daniel Friedrich, Ioannis Spanopoulos, Justin Hoffman,
Vinayak Dravid, et al.

▶ To cite this version:

Eugenia Vasileiadou, Ido Hadar, Mikael Kepenekian, Jacky Even, Qing Tu, et al.. Shedding Light on the Stability and Structure–Property Relationships of Two-Dimensional Hybrid Lead Bromide Perovskites. Chemistry of Materials, 2021, 33 (13), pp.5085-5107. 10.1021/acs.chemmater.1c01129 . hal-03270812

HAL Id: hal-03270812
https://hal.science/hal-03270812

Submitted on 16 May 2023

Shedding Light on the Stability and Structure–Property Relationships of Two-Dimensional Hybrid Lead Bromide Perovskites

Eugenia S. Vasileiadou, Ido Hadar, Mikaël Kepenekian, Jacky Even, Qing Tu, Christos D. Malliakas,
Daniel Friedrich, Ioannis Spanopoulos, Justin M. Hoffman, Vinayak P. Dravid,
and Mercouri G. Kanatzidis*

ABSTRACT: Two-dimensional (2D) hybrid lead iodide perovskites have gained prominence due to their remarkable structural tunability, optoelectronic features, and moisture stability, which have rendered them as attractive alternatives to 3D $MAPbI_3$ for optoelectronic devices. 2D multilayer lead bromide perovskites remain an unfathomed phase space with the lack of systematic studies to establish the structure, photophysical properties and stability behavior of this family of 2D halide perovskites. Herein, we present new members of bilayer lead bromide perovskites $(C_mH_{2m+1}NH_3)_2(CH_3NH_3)Pb_2Br_7$ (m = 6–8) that belong to the Ruddlesden–Popper structure type, incorporating long chain alkyl-monoammonium cations ($C_mH_{2m+1}NH_3$) of hexylammonium (m = 6), heptylammonium (m = 7), and octylammonium (m = 8). A universal solution synthetic methodology for bulk multilayer lead bromide perovskites is presented with all structures solved and refined using single crystal X-ray diffraction. The studied bilayer lead bromide perovskites demonstrate a decrease in the lattice rigidity and lattice match of the inorganic perovskite layer–organic layer, as the alkyl-monoammonium chain length increases. In comparison to their iodide analogues, the bilayer lead bromide compounds exhibit elongation of their stacking axis despite the smaller dimensions of the $[PbBr_6]^{4-}$ lattice, while their internal lattice strain was calculated to be reduced, inferring a greater lattice match between the inorganic $[PbBr_6]^{4-}$ perovskite layer and organic layer. The $(C_mH_{2m+1}NH_3)_2(CH_3NH_3)Pb_2Br_7$ (m = 4, 6–8) compounds exhibit narrow-band emission near 2.5 eV. Time-resolved photoluminescence (PL) displays longer carrier lifetimes on the nanosecond time scale comparing to their iodide analogues, where electronic structure calculations indicate that the increase of the alkyl chain length and, thus, lattice softness enhances nonradiative recombinations. A complete set of air, light, and heat stability tests on unencapsulated thin films of $(C_mH_{2m+1}NH_3)_2(CH_3NH_3)Pb_2Br_7$ (m = 4, 6–8) and $MAPbBr_3$ show they are stable in ambient air for at least 5 months, exhibiting greater extrinsic stability than the 2D lead iodide congeners. Extraordinarily, 3D $MAPbBr_3$ films prove to be more stable than films of 2D lead bromide perovskites, in contrast to $MAPbI_3$ which is less stable than the 2D lead iodide perovskites.

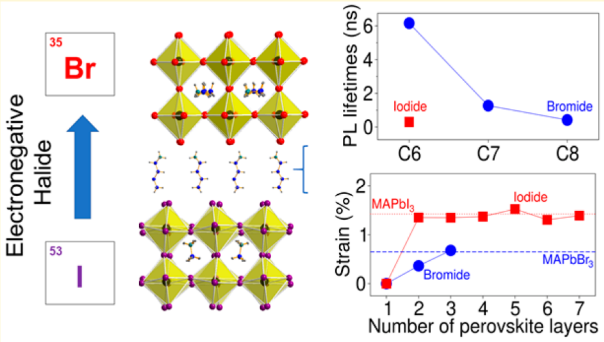

■ INTRODUCTION

Hybrid organic–inorganic halide perovskites are emerging semiconductor materials for a broad range of optoelectronic applications such as photovoltaics and light-emitting diodes (LEDs) due to their surprising high tolerance to defects and desirable optical properties (e.g., carrier lifetimes, long diffusion lengths).[1−5] Additionally, these soft materials are synthesized using scalable solution processes that are inexpensive and versatile, compared to conventional semiconductors such as Si, Ge, and GaAs.[3,6−10] The general chemical formula for the 3D halide perovskite structure is AMX_3 where A is one of following monovalent cations: $CH_3NH_3^+$ (MA^+), $HC(NH_2)_2^+$ (FA^+), Cs^+, or recently $CH_3NH_2NH_2^+$ [11,12], while M is a divalent cation (here Ge^{2+}, Sn^{2+}, Pb^{2+}) and X is a halide (Cl^-, Br^-, or I^-). The compositional tailoring of the 3D structure is restricted by the geometric Goldschmidt's tolerance factor.[13,14] Lately, the lower dimensional −2D multilayer lead iodide perovskites have emerged as accentuating alternatives to the 3D parent material $MAPbI_3$, due to improved moisture stability and higher structural flexibility that permits a much greater compositional space to engineer new materials.[15−21]

Conceptually, 2D hybrid halide perovskites can be imagined as derived from the 3D structure by slicing along specific crystallographic directions, most commonly the [100] direction, giving the general formula of $(A')_m(A)_{n-1}M_nX_{3n+1}$, in which A′ is a monovalent ($m = 2$) or divalent ($m = 1$) cation and n is the thickness of inorganic layers.[7,21−23] The 2D structure consists of the anionic network of corner-sharing $[MX_6]^{4-}$ octahedra, with the A-site cation sitting in the center between the cuboctahedral cavities. 2D Wannier excitons with high binding energy are stabilized because of the dimensional reduction, which are observed even at ambient temperatures.[24,25] Hence, the layered 2D perovskite structure permits both coarse and fine-tuning of the optoelectronic properties, enhancing their potential for technological applications.[24,25] Lately, numerous studies have examined 2D hybrid lead iodide perovskites, focusing mainly on these materials as thin films and in bulk.[15,22,26−35] An initial fundamental understanding of 2D lead iodide perovskites' structure, properties, and device refinement has been developed.[19,29,36−56] However, the 2D lead bromide analogues are comparatively underexplored, and there is no comprehensive analysis on the structure−property relationship of the multilayer members of this family of materials. A few results nevertheless indicate that optical tunability and homogeneous emission lines may be obtained when using halide binary alloys thanks to the robustness of the 2D Wannier exciton for the [100] orientation.[57] Synthetically, the majority of the materials reported are monolayer ($n = 1$) 2D bromide perovskites.[37,58−76] A significant amount of the studied monolayer lead bromide perovskites adopt the [110] orientation, which exhibit broadband emission due to photogenerated energy distribution of self-trapped exciton states that are associated with the distortion of the [110] corrugated structure.[77−89]

The only studied bulk, multilayer lead bromide perovskites are based on the common short guanidinium, ethylammonium, propylammonium, and butylammonium, as well as one reference with hexylammonium, as the A′-site spacer cation, tuned to give n = 2 or 3 layer members, but single-crystal structural data is scarce.[81,90−100] Specifically, 2D perovskites incorporating butylammonium-based cations include $(CH_3(CH_2)_3NH_3)_2(MA)_{n-1}Pb_nBr_{3n+1}$ (n = 1−3), $(CH_3(CH_2)_3NH_3)_2(FA)Pb_2Br_7$, $(CH_3(CH_2)_3NH_3)_2(Cs)Pb_2Br_7$, $(CH_3(CH_2)_3NH_3)_2(Cs)Pb_3Br_{10}$, and $((CH_3)_2CHCH_2NH_3)_2(CH_3\ CH_2NH_3)Pb_2Br_7$ with isobutylammonium $(CH_3)_2CHCH_2NH_3$.[91,94−99,101,102] The 2D lead bromide perovskites incorporating ethylammonium-based cations include $(C_2H_8N)_4Pb_3Br_{10}$, a unique three-layered perovskite with [100] orientation where ethylammonium occupies both A- and A′-site cation positions, and the [110]-orientated perovskite with hydroxyethylammonium $(HO-(CH_2)_2NH_3)_2(FA)_2Pb_2Br_8$.[81,85] Recently, a report of 2D hybrid lead bromide perovskites of the Dion−Jacobson structure described incorporating cyclic diammonium cations.[103] Moreover, most of these 2D lead bromide perovskites examined report ferroelectricity as a property.[68,69,73,74,91,94−98,104−110]

The research on multilayer lead bromide perovskites is less well-developed compared to the lead iodides, which demands a fundamental and holistic study of this family of materials. Despite the rapid advancement and applications of hybrid perovskite materials, there has not been a systematic investigation to examine the structure, stability, and photophysical properties of multilayer lead bromide perovskites. In addition, there is no comparative study inspecting the differences with the 2D lead iodide analogues. Furthermore, the environmental stability of 2D lead bromide perovskites is unestablished, as well as in comparison with the 3D $MAPbBr_3$. Considering the above, it is important to explore and characterize the available structural phase space to rationalize the fundamental structure−property relationship in 2D lead bromide perovskites and utilize their potential along with the iodide analogues. Studying the intrinsic properties of these materials in both bulk single-crystal and thin films is important for luminescent device applications. Remarkably, within a short period of time green light-emitting diodes (LEDs) consisting of quasi 2D/3D and layered lead bromide perovskites have demonstrated an unprecedented surge with high current and brightness and external quantum efficiency up to 20%.[111−121] The photophysical origins of the attractive performances are still under study. The high exciton binding energy and reduced electron−phonon coupling have been suggested to promote radiative recombination pathways.[117,122] On the other hand, the reduction of internal strain in 2D multilayer perovskites allows the acquisition of higher n values[123,124] and is favored by the softness of the organic barrier layer containing the spacer cations, as well as a small internal lattice mismatch.[125] Therefore, the optimization of multilayer halide perovskites with suitable optoelectronic properties requires a fine-tuning of the material components. Structural analysis of the bulk materials offers the needed atomic level detail that can direct the understanding of these materials' photophysics and device engineering.

In this work, we report the successful synthesis and crystallographic characterization of 2D bilayer lead bromide perovskites incorporating straight chain aliphatic monoammonium cations: $(C_mH_{2m+1}NH_3)_2(CH_3NH_3)Pb_2Br_7$ (m = 6−8). We rationally expand the 2D Ruddlesden−Popper perovskite bromide family to establish the structure, properties, and environmental stability by systematically tuning the length of the organic spacer cation. For this purpose, we use the organic spacers hexylamine (m = 6, C6), heptylamine (m = 7, C7), and octylamine (m = 8, C8) increasing in this way by two, three, and four carbons, respectively, to the reference 2D bilayer bromide materials of butylamine (m = 4, C4). A universal synthetic methodology for multilayer lead bromide perovskites is proposed. The optical properties of the studied 2D materials show a narrow-band emission above the range of 2.5 eV, suitable for light-emission applications. The photoluminescence (PL) lifetimes demonstrate long carrier lifetimes on the nanoscale time scale, whereas the lead iodide congeners exhibit shorter carrier lifetimes on the picosecond time scale.[34] Electronic band structure calculations of the newly reported structures show a nearly direct bandgap, while the carrier effective mass remains larger than in the corresponding iodide structures. Collectively, the experimental structural and photophysical information along with the theoretical calculations postulate that a greater lattice rigidity is compensated by a smaller internal lattice strain, allowing the formation of multilayer 2D perovskite structures, which simultaneously limits the nonradiative recombinations. These aspects are illustrated by analyzing the role of the halide anion and the length of alkylammonium chain. Furthermore, the methodical assessment of the environmental stability of thin films of $(C_mH_{2m+1}NH_3)_2(CH_3NH_3)Pb_2Br_7$ (m = 4, 6−8) reveals that the extrinsic stability to air, heat, and light increases with the length of the organic spacer cation, while the studied 2D lead bromide perovskites show greater extrinsic stability to their 2D iodide congeners. In comparison $MAPbBr_3$ manifests superior stability over both 2D lead bromide and lead iodide perovskites under operating conditions. Switching spectroscopy piezoresponse force microscopy (SS-PFM) on the studied materials' thin film surface reveals a hysteretic behavior typical for ferroelectric polarization switching. Altogether, this study informs our fundamental understanding of the structure and properties of multilayer 2D hybrid lead bromide perovskites and reveals pronounced differences with the 2D lead iodide perovskites congeners.

■ EXPERIMENTAL SECTION

All starting materials for synthesis were purchased commercially and were used without further purification, except for methylamine hydrochloride which was dried in an oven at 70 °C. PbO (99.9%), hydrobromic acid (ACS reagent, 48 wt % in H_2O), and hypophosphorous acid solution (50 wt % in H_2O) were purchased from Sigma-Aldrich and used as received. The following amines—hexylamine (99%), heptylamine (99%), and octylamine (99%)—were purchased from Sigma-Aldrich and used as received. Methylammonium hydrochloride ⩾98% (CH_3NH_2·HCl = MACl) was purchased from Sigma-Aldrich and stored in an oven.

Synthesis of $(C_4H_{12}N)_2(MA)Pb_2Br_7$. PbO (2 mmol; 446.4 mg) and MACl (1 mmol; 67.5 mg) powders were dissolved in 5 mL of hydrobromic acid (HBr) by heating to boiling under constant magnetic stirring, until a clear, transparent solution was obtained. Next, in a separate vial, 197 μL (2 mmol) of butylamine ($C_4H_9NH_2$) were added to 50% aqueous H_3PO_2 (0.5 mL). The use of the weak acid H_3PO_2 in the synthesis serves the practical purpose of protonating the basic, organic spacer amine before its addition into the strongly acidic HBr solution, so that no strong exothermic reaction occurs with the addition of the organic amine, while the added amount of amine is intact. The following solution was added to the reaction solution, under continuous stirring and heating. After 10−15 min, the stirring was stopped and the hot plate was turned off. The reaction solution was left to cool to room temperature, and bright, yellow crystals precipitated from the solution. The crystals were isolated by vacuum filtration and dried under vacuum overnight. Yield 300 mg (67.3% based on Pb).

Synthesis of $(C_6H_{16}N)_2(MA)Pb_2Br_7$. PbO (2 mmol; 446.4 mg) and MACl (1 mmol; 67.5 mg) powders were dissolved in 6 mL of hydrobromic acid (HBr) by heating to boiling under constant magnetic stirring, until a clear, transparent solution was obtained. Next, in a separate vial, 127 μL (1 mmol) of hexylamine ($C_6H_{13}NH_2$) was added to 50% aqueous H_3PO_2 (0.5 mL). The following solution was added to the reaction solution, under continuous stirring and heating. After 10−15 min, stirring was stopped, the temperature was lowered to 120 °C (as indicated on hot plate), below the boiling point of HBr and kept constant for several days until the first light-yellow crystals seeds started to grow. The temperature was decreased to 95 °C (as indicated on hot plate) and kept constant for several days to induce stronger precipitation and faster crystal growth. Following this, the hot plate was turned off and the reaction solution was left to cool to room temperature for the completion of the precipitation and crystal growth. The crystals were isolated by vacuum filtration and dried under vacuum overnight. Yield 230 mg (52% based on Pb).

Synthesis of $(C_7H_{18}N)_2(MA)Pb_2Br_7$. PbO (2 mmol; 446.4 mg) and MACl (1 mmol; 70 mg) powders were dissolved in 6.5 mL of HBr by heating to boiling under constant magnetic stirring, until a clear, transparent solution was obtained. Next, in a separate vial, 78 μL (0.5 mmol) of heptylamine ($C_7H_{15}NH_2$) were added to 50% aqueous H_3PO_2 (0.5 mL). The following solution was added to the reaction solution, under continuous stirring and heating. After a couple of minutes (10−15 min), stirring was stopped, the temperature was lowered to 120 °C (as indicated on hot plate), and the same crystal growth−cooling cycle was followed as was for the $(C_6H_{16}N)_2(MA)Pb_2Br_7$ synthesis. Yield 198 mg (44% based on Pb).

Synthesis of $(C_8H_{20}N)_2(MA)Pb_2Br_7$. PbO (2 mmol; 446.4 mg) and MACl (2 mmol; 135 mg) powders were dissolved in 10 mL of HBr by heating to boiling under constant magnetic stirring, until a clear, transparent solution was obtained. Next, in a separate vial, 41 μL (0.25 mmol) of octylamine ($C_8H_{17}NH_2$) was added to 50% aqueous H_3PO_2 (0.5 mL). The following solution was added to the reaction solution, under continuous stirring and heating. After a couple of minutes (10−15 min), stirring was stopped, the temperature was lowered to 120 °C (as indicated on hot plate), and the same crystal growth−cooling cycle was followed as was for the $(C_6H_{16}N)_2(MA)Pb_2Br_7$ synthesis. Yield 202 mg (45% based on Pb).

Film Fabrication. ITO glass substrates were first cleaned by sequential sonication in aqueous detergent, water, acetone, and isopropanol for 20 min each. Afterward, substrates were blown dry with nitrogen. Then, the substrates were treated for 30 min using the ultraviolet ozone (UVO) treatment method.

One-Step Method. Solutions of the studied materials were prepared by dissolving 100 mg of the dried crystals in 200 μL of anhydrous DMF solvent. The precursor solution was injected onto the substrate and spin-coated at a speed of 5000 rpm for 30 s in ambient air. Afterward, the resulting films were annealed at 110 °C on a hot plate for 10 min in ambient air. For films fabricated in the glovebox under an N_2 atmosphere, the spin-coating and annealing steps were undertaken in the glovebox.

Hot-Casting Method. Solutions of the studied materials were prepared by dissolving 100 mg of the dried crystals in 200 μL of anhydrous DMF solvent. The substrates were heated at 110 °C on a hot plate for 10 min in ambient air. Afterward, the precursor solution was injected onto the substrate and spin-coated at a speed of 5000 rpm for 30 s in ambient air. For films fabricated in the glovebox under an N_2 atmosphere, the annealing and spin-coating steps were undertaken in the glovebox.

Characterization. The broad battery of experimental techniques and methods used for the characterization of the structure and properties of the studied materials are found in detail in the Supporting Information (SI).

■ RESULTS AND DISCUSSION

Synthetic Aspects. The synthesis of the new members of bilayer lead bromide perovskites $(C_mH_{2m+1}N)_2(MA)Pb_2Br_7$ (m = 6−8: **C6BrN2**, **C7BrN2**, and **C8BrN2**, respectively) with straight, long-chain aliphatic alkyl-monoammonium cations, is challenging compared to the previously reported compounds with the shorter butylammonium cation[91,94−98] due to the lower solubility of the long-chain monoammonium cations in HBr, which can lead to a mixture of 2D perovskites with different numbers of inorganic layers (n). The targeted synthesis of the studied bilayer lead bromide perovskites is based on the solution method previously developed by our group for phase-pure synthesis of 2D multilayer lead iodide perovskites.[10,27,34] Briefly, a stoichiometric amount of PbO/MACl (Pb^{2+}/MA^+) is used, where the concentration of the organic spacer is varied until a solution of pure product is obtained with the desired n value (e.g., n = 2) in an appropriate volume of hydrohalic acid, under stirring and heating.[34] The formula governing the acquisition of the pure product is the ratio of the spacer amine to the overall concentration of the hydrohalic solution under a fixed Pb^{2+}/MA^+ ratio. The solubility limit for $MAPbBr_3$ in HBr is ∼0.56 M at boiling point, and the Pb^{2+}/MA^+ concentration needs to be adjusted to it, while the HBr volume must be large enough to dissolve the n = 1 compound. Specifically, for the same stoichiometric amount of Pb^{2+}/MA^+ (2:1 mmol) used, the amount of spacer needed (C4, C6, and C7) decreases drastically with the increase of the hydrocarbon chain length. This means that smaller concentration of an organic spacer can be used for longer chain amines because of the decreasing solubility of the resultant products. Specifically, for the targeted synthesis of these bilayer perovskites: 1 mmol of C6 in 6 mL HBr is needed for synthesis of C6BrN2 (instead of the stoichiometric 2 mmol of C6), 0.5 mmol of C7 in 6.5 mL for C7BrN2, and 0.25 mmol of C8 in 10 mL for C8BrN2 is needed. In contrast, for $(C_4H_{12}N)_2(MA)Pb_2Br_7$ (**C4BrN2**) the stoichiometric amount achieves pure-phase synthesis with 2 mmol of C4 in 5 mL HBr.

It is worth noting for the targeted synthesis of C8BrN2, besides the less than stoichiometric amount of organic spacer needed, the required ratio of Pb^{2+}/MA^{+} is 1:1, versus the stoichiometric 2:1. This is because the ratio of octylammonium cation has a greater insolubility to the overall HBr solution concentration, which requires a higher Pb^{2+}/MA^{+} concentration to result in the $n = 2$ perovskite as the majority product. The attempts with a 2:1 ratio of Pb^{2+}/MA^{+} with 0.25 mmol of C8 in 10 mL HBr yielded significant $n = 1$ impurity. The $n = 1$ perovskite appears due to the lower solubility of the longer alkyl-monoammonium cation in hydrohalic acid, related to the higher reactivity of the longer hydrocarbon chain. The same results arose from variation of octylammonium concentration in HBr with the steady 2:1 ratio of Pb^{2+}/MA^{+}. This indicates the synthetic challenges of using hydrohalic acid for a targeted synthesis of multilayer lead halide perovskites with the incorporation of insoluble and lengthy monoammonium cations greater than C8.

Furthermore, an important parameter controlling the synthetic outcome of a uniform phase product with long chain amines is the temperature cooling profile. If the reaction solutions are left to freely cool at room temperature (R.T.), a mixture of different numbers of inorganic layers (n) is usually obtained. This is vividly apparent in the cases of C7BrN2 and C8BrN2, where $n = 1$ product is always obtained unless the reaction is cooled carefully and stepwise, over multiple days. Additionally, the quality and morphology of the crystals is significantly improved with stepwise cooling temperature profiles, where less twinning is observed. Accordingly, after the subsequent addition of all the reagents together and once a clear solution is formed, the temperature is lowered to slightly below the boiling point of HBr to 120 °C (as indicated on a hot plate). The solution is held at this temperature for several days under reflux to avoid the formation of other n-layer members. Once the light-yellow crystal seeding starts, the reaction solution is lowered to 95 °C (as indicated on a hot plate) and left for a couple of days for crystal growth. Finally, the hot plate is turned off for full crystal precipitation to be achieved, as the reaction solution is left to slowly cool to room temperature. The crystals are dried from the reaction solution by vacuum filtration, which needs to be supervised and brief (∼10 min); otherwise, an orange layer can form on the crystals, which we associate to $MAPbBr_3$ residue. Following careful vacuum filtration, the crystals are left under vacuum in a desiccator overnight. Upon drying, the bulk crystals exhibit excellent stability in ambient conditions. As seen in Figure S2−5, all the experimental diffraction patterns match to the calculated diffraction patterns from the solved single-crystal structures, verifying the successful synthesis of the targeted bilayer perovskites.

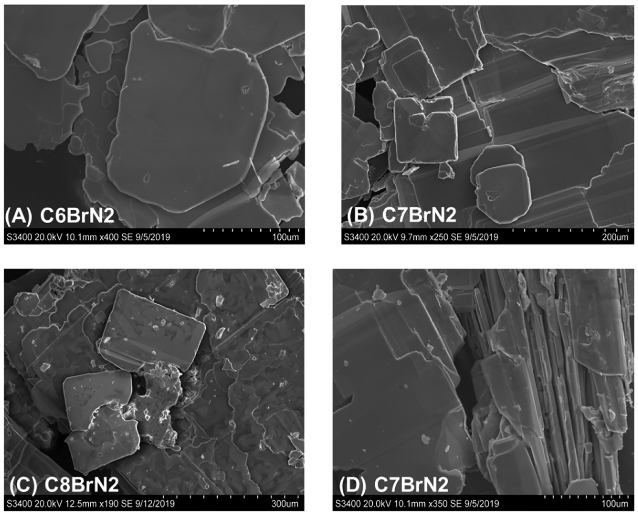

Figure 1. SEM images of crystals of (**A**) C6BrN2, (**B**) C7BrN2, and (**C**) C8BrN2 and (**D**) SEM image presenting the thickness of consecutively stacked crystals of C7BrN2.

Scanning electron microscopy (SEM) studies reveals a plate-like shape of the single crystals and stacking-layered morphology for all studied materials, as shown in Figure 1, which is a distinctive characteristic for the 2D layered structure.[10] The crystals formed for all three novel compounds (C6BrN2, C7BrN2, and C8BrN2) are delicately thin, easily stack on top of each other to form "mountains" of multiple crystals (Figure S1), and have a brittle nature in comparison to C4BrN2 crystals' morphology. The stacking can be seen in Figure 1D, showing crystals of C7BrN2 that have naturally stacked on top of each other consecutively, and the thickness of each crystal can be estimated around 10 μm. In contrast, the bilayer lead iodide perovskites reported with the same spacers of C4 and C6 form crystals of thicker morphology, based on empirical and SEM comparison.[10,34] It would be of interest to evaluate the mechanical properties of multilayer lead bromide perovskites, to compare with the reported studies of lead iodide perovskites.[126−129]

Considering the above, we now have a practically universal solution synthesis method for uniform phase 2D multilayer lead bromide perovskites, employing the solution synthesis method based on hydrohalic acid. Thus, this methodology can be a synthetic basis for the further exploration of the 2D lead bromide perovskite family. It is possible to tailor this solution synthetic methodology to other diverse systems of organic spacer molecules in order to find the suitable concentration of spacer cation needed to result in bulk, uniform pure 2D multilayer lead bromide perovskites with $n > 1$.

Description of Crystal Structures. The crystal structures of all studied compounds were solved from single crystal X-ray diffraction (SCXRD) data collected at room temperature for C7BrN2 and C8BrN2. The crystal structure of C6BrN2 was collected at 0 °C to eliminate the influence of a phase transition at 30 °C (see more details in the Thermal Properties section). These crystalline phases represent new members of 2D Ruddlesden−Popper (RP) perovskites with inorganic layers $[Pb_2Br_7]^{3-}$ consisting of corner-sharing $[PbBr_6]^{4-}$ octahedra which are separated by the organic spacer cations in the [100] direction (Figure 2). All studied compounds crystallize in the monoclinic crystal space group Cc (Table 1). This structural behavior of crystal symmetry preference in the studied bilayer lead bromide perovskites is consistent with the crystal symmetry preference of the reported bilayer lead iodide perovskite analogues with the butylammonium and hexylam-

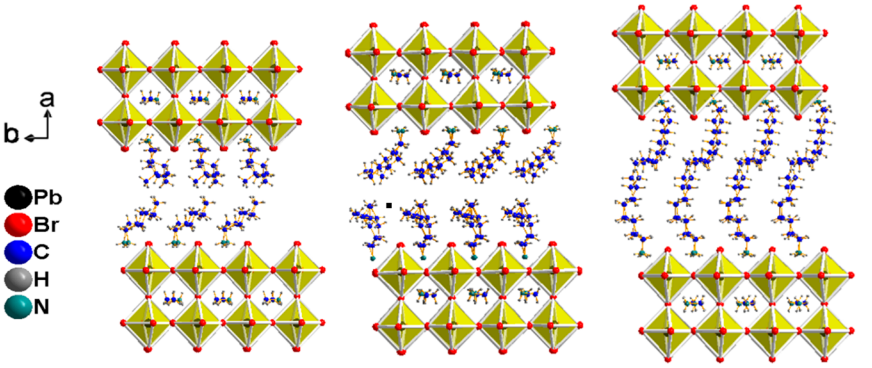

$(C_6H_{13}NH_3)_2(CH_3NH_3)Pb_2Br_7$ $(C_7H_{15}NH_3)_2(CH_3NH_3)Pb_2Br_7$ $(C_8H_{17}NH_3)_2(CH_3NH_3)Pb_2Br_7$

Figure 2. Depiction of C6BrN2, C7BrN2, and C8BrN2 structures solved from single crystal X-ray diffraction data.

Table 1. Crystal Data and Structure Refinement for $(C_mH_{2m+1}NH_3)_2(CH_3NH_3)Pb_2Br_7$ (m = 6−8)

	C6BrN2	C7BrN2	C8BrN2
empirical formula	$C_{13}H_{38}N_3Pb_2Br_7$	$C_{15}H_{42}N_3Pb_2Br_7$	$C_{17}H_{46}N_3Pb_2Br_7$
formula weight	1210.2	1235.2	1266.32
temperature (K)	273.01	296.99	296.15
crystal system	monoclinic	monoclinic	monoclinic
space group	*Cc*	*Cc*	*Cc*
crystal shape	plate	plate	plate
crystal color	light yellow	light yellow	light yellow
unit cell dimensions (Å)	a = 46.069(5)	a = 49.4930(15)	a = 52.952(5)
	b = 8.2722(5)	b = 8.3269(2)	b = 8.3232(7)
	c = 8.3454(12)	c = 8.3253(2)	c = 8.3225(7)
	β = 90.852(17)°	β = 90.008(2)°	β = 90.010(2)°
volume (Å^3)	3180.0(6)	3431.05(16)	3668.0(5)
Z	4	4	4
density (calculated, g/cm^3)	2.5277	2.3912	2.293
reflections collected	10873	12136	40438
independent reflections	5951 [R_{int} = 0.034]	7051 [R_{int} = 0.0553]	12154 [R_{int} = 0.0769]
completeness to θ = 29.27°	96%	98%	100%
data/restraints/parameters	5951/23/133	7051/26/139	12154/52/152
goodness-of-fit	2.11	2.21	1.001
final R indices [$I > 3\sigma(I)$][a]	R_{obs} = 0.0897, wR_{obs} = 0.1882	R_{obs} = 0.0588, wR_{obs} = 0.1604	R_{obs} = 0.0717, wR_{obs} = 0.1936
R indices [all data]	R_{all} = 0.1832, wR_{all} = 0.2068	R_{all} = 0.1035, wR_{all} = 0.1690	R_{all} = 0.1490, wR_{all} = 0.2333
largest diff. peak and hole (e·Å^{-3})	2.92 and −1.08	2.15 and −1.16	2.262 and −2.067

[a] $R = \sum||F_o| - |F_c||/\sum|F_o|$, $wR = (\sum[w(|F_o|^2 - |F_c|^2)^2]/\sum[w(|F_o|^4)])^{1/2}$, and $iw = 1/(\sigma^2(I) + 0.0004I^2)$.

monium cations.[10,34] We used the recommended "Hamilton significance test" on the crystallographic R factor to support the choice of a noncentrosymmetric space group for C6BrN2.[130] An R-factor ratio (R) is calculated, equal to $R = wR_2/wR_1$ where wR_1 is the structure resulting from the better of the two absolute configurations and wR_2 for the alternative configuration.[130] Then, a calculated R-factor (R_{calc}) ratio is derived from the tables for testing the R-factor at significance level 0.05*C*. Lastly, comparing R and R_{calc} for C6BrN2, we found $R > R_{calc}$ which means we can reject the hypothesis that the alternative configuration is correct at the 95% level of significance. An additional validation of the space group assignment comes from DFT calculations (see below), where the *Cc* structure appears to be more stable than the *C*2/*c* at ΔE = 0.206 eV/f.u. As such, 2D lead bromide perovskites incorporating straight chain aliphatic alkyl-monoammonium cations as the organic spacer have lower symmetry in comparison with the crystal structure of C4BrN2 that was reported to crystallize in the orthorhombic space group *Cmc*2$_1$ at 200 K.[96] Thus, the new n = 2 members described here expand the structural information known for this underexplored phase space of 2D multilayer bromide perovskites.

The unit cell of the titled 2D perovskites consists of one long stacking a axis and two shorter in-plane b, c axes. The length of the trans Br−Pb−Br unit is approximately 5.8 Å, which makes up the length of one $[PbBr_6]^{4-}$ octahedron of the inorganic layer. For a primitive unit cell, the length of the stacking axis can be defined: $5.8n + x$, where n is the number of inorganic layers and x is the separation between the inorganic layers and, thus, the length of the organic spacer molecule. The long monoammonium organic spacers interact noncovalently with the inorganic layers that create a staggered arrangement of the successive inorganic layers. The offset of the adjacent inorganic layers is (0.5, 0.5), thus displaying the Ruddlesden−Popper (RP) structure type.

Assessing the structures of the n = 2 compounds, which have the same inorganic layers but different organic spacer molecules, allows us to investigate the influence of the organic spacer monoamine on the structural characteristics and properties of 2D bromide perovskites. Increasing the length

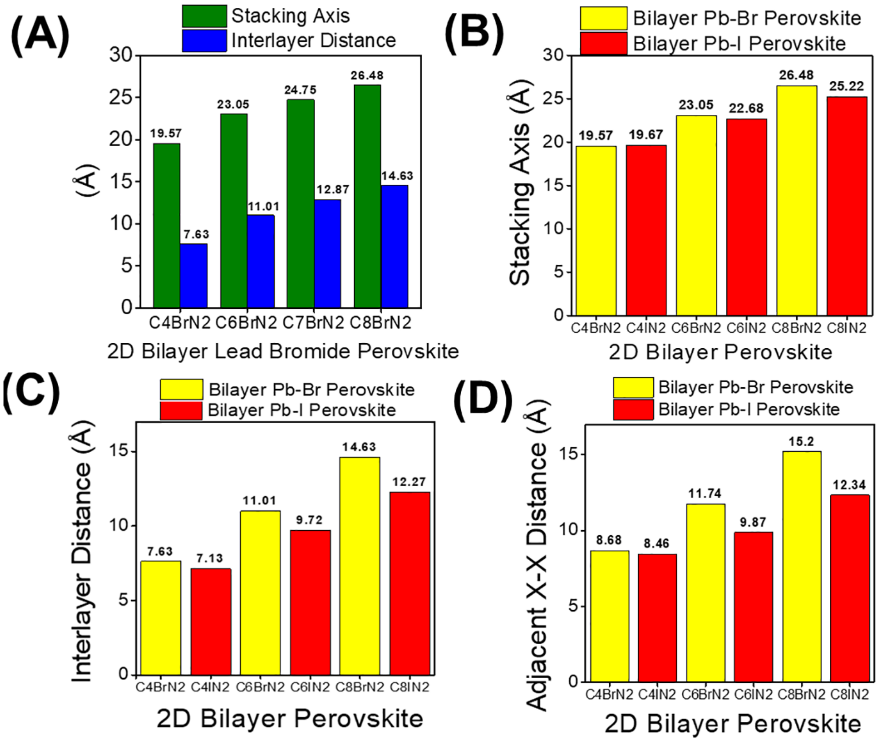

Figure 3. (**A**) Comparison of stacking axis and interlayer distance from crystal structures of 2D lead bromide perovskites C4BrN2, C6BrN2, C7BrN2, and C8BrN2. (**B**) Comparison of stacking axis, (**C**) interlayer distance, and (**D**) adjacent X−X (X = halide) distance from crystal structures of 2D lead bromide perovskites C4BrN2, C6BrN2, and C8BrN2 versus 2D lead iodide perovskites C4IN2, C6IN2, and C8IN2.

of the straight chain aliphatic monoammonium spacer leads to the expected uniaxial expansion of the layer stacking axis, as well as the increase of the interlayer distance (defined as the distance between the planes passing through the terminal bromine atoms of the adjacent $[PbBr_6]^{4-}$ layers) between the inorganic lead bromide layers from 7.63 Å for C4BrN2 to 11.01 Å for C6BrN2, 12.87 Å for C7BrN2, and 14.63 Å for C8BrN2 (Figure 3A).

Comparison of 2D Bilayer Lead Bromide and Lead Iodide Perovskites. The stacking axis of the studied bilayer lead bromide perovskites ranges from 19.57 Å for C4BrN2 up to 26.48 Å for C8BrN2 (Figure 3A). It is noteworthy to draw comparison to the published structures of the bilayer lead iodide analogues:[10,34] $(C_4H_{12}NH_3)_2(CH_3NH_3)Pb_2I_7$ symbolized from here on as **C4IN2**, $(C_6H_{16}NH_3)_2(CH_3NH_3)Pb_2I_7$ as **C6IN2**, and finally $(C_8H_{20}NH_3)_2(CH_3NH_3)Pb_2I_7$ as **C8IN2**, where the C8IN2 single crystal structure is reported here, originally. We previously reported the synthesis and photophysical characterization of the C8NI2 compound which is the reason we readily reproduced it here in our comparative study,[131] whereas $(C_7H_{18}NH_3)_2(CH_3NH_3)Pb_2I_7$ remains unstudied. The stacking axis of all six compounds in comparison can be seen in Figure 3B. The stacking axis value of C4BrN2 is 19.57 Å versus 19.67 Å for C4IN2, where there is a negligible difference. However, for the extended long chain amines, there is a notable difference: 23.05 Å for C6BrN2 versus 22.68 Å for C6IN2 and 26.48 Å for C8BrN2 versus 25.22 Å for C8IN2. Hence, the bromide analogues have a longer stacking axis in comparison to their iodide analogues, and there seems to be a significant increase in this difference, from 0.37 Å difference between the C6 analogues to 1.26 Å difference between the C8 analogues (Figure 3B).

Interestingly, construing the origin of the larger stacking axis in the bromide versus iodide analogues allows a comparison in the strength of the electrostatic interactions of the alkylmonoammonium chains between the two types of inorganic layers. The $[PbBr_6]^{4-}$ octahedra in the inorganic layers are smaller than the $[PbI_6]^{4-}$ octahedra due to the shorter bond length of Pb−Br (average 2.97 Å), in comparison to Pb−I (average 3.1 Å). Further, the dimensions are consistently smaller in the in-plane direction along the *b* and *c* axes for C4BrN2, C6BrN2, and C8BrN2 in comparison to the iodide analogues, while the volume and density also remain smaller in the bromides (Table S1). Thus, it would be expected similarly that the stacking axis in the bromide analogues would be consistently smaller than the iodide analogues. Nonetheless, this is not the case for the C6BrN2 and C8BrN2 compounds (Figure 3B and 4). Based on the comparison of the structural parameters from single-crystal structures, it seems that the steric and electrostatic interactions of the elongated C6 and C8 organic cations accommodate a laterally interdigitated conformation of their alkyl tails between the $[PbBr_6]^{4-}$ octahedra, in contrast to that between the $[PbI_6]^{4-}$ octahedra. It appears that increasing the monoammonium cation's length accentuates this phenomenon for the integrity of the 2D structure in the bilayer lead bromide perovskites to be maintained. Ultimately, this is expressed in the axial elongation of the stacking axis of bromide versus the iodide analogues (Figure 3B) while the equatorial dimensions and volume of the hybrid bromide lattice remain expectedly compact (Table S1). Analogously, this is also reflected in the elongation of the interlayer distance between the inorganic layers of the bromide perovskites versus the iodide congeners (Figure 3C), as well as the distance between the adjacent halogen atoms of the inorganic layers (Figure 3D). The preferred stereochemical

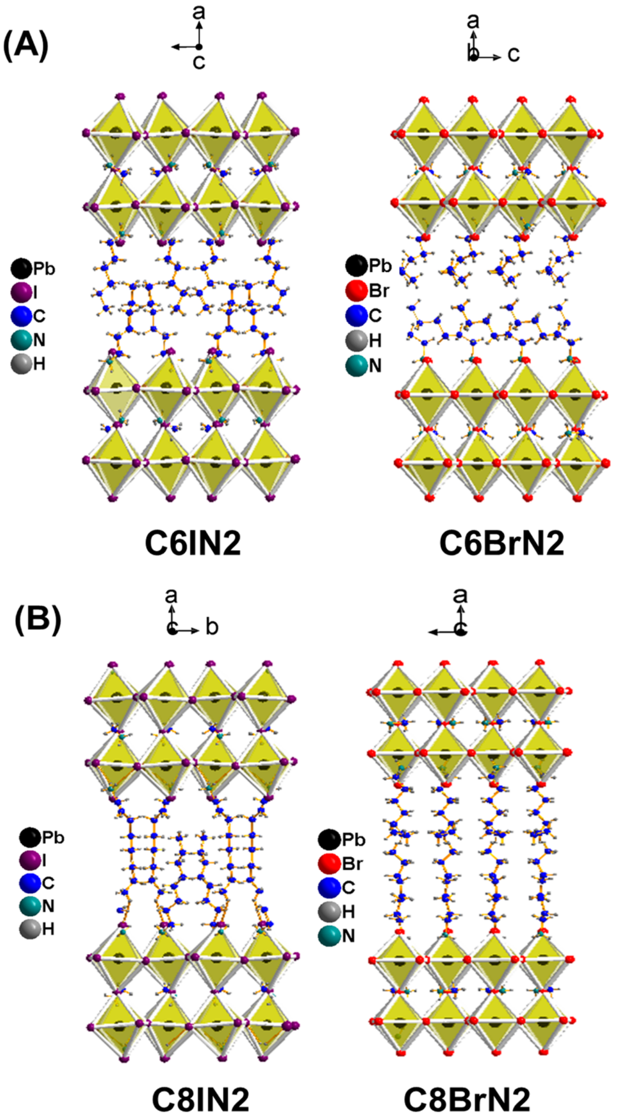

Figure 4. (**A**) Comparison of the crystal structures of C6IN2 and C6BrN2. (**B**) Comparison of the crystal structures of C8IN2 and C8BrN2.

conformation of the organic cations that leads to a greater lateral interdigitation in the bromide analogues demonstrates that the directed synthetic design can structurally regulate the interlayer distance by controlling: (i) the packing morphology of the organic spacer cation and (ii) the steric-electrostatic interactions of the organic cation with the inorganic lattice. In regard to the latter, increasing the strength of the steric-electrostatic interactions by maintaining a constant organic spacer and tuning the inorganic lattice to a more electronegative halide anion was applied as a synthetic strategy recently in RP double halide perovskites and n = 1 single-metal halide perovskites.[132]

Furthermore, the distortion levels of the inorganic octahedra assessed through the bridging Pb−X−Pb angles are associated with the bandgap of the materials.[28,31,103,133−135] We can classify the Pb−Br−Pb angles into two classes, the equatorial angle (parallel to the inorganic plane) and the axial angle (in the stacking direction) (Figure 5). In the novel n = 2 compounds studied here, the axial Pb−Br−Pb angles are close to 180°, which reflects minor distortion of the inorganic layers in this direction (Figure 6A). Conversely, the equatorial Pb−Br−Pb angles deviate significantly from 180°, which contributes significantly to the bandgap value.[96−98] On average, C6BrN2 consistently has the largest distortions of the three newly reported bromide compounds, with an average equilateral angle 161.82°, whereas C7BrN2 and C8BrN2 have similar values with C7BrN2 having an average equilateral angle of 166.20° and C8BrN2 has an average equilateral angle of 165.72° (Figure 6B).

The bond angle variance (calculated from the formula $\sigma^2 = \sum_{i=1}^{12} \frac{(\theta_i - 90)^2}{11}$) of the individual $[PbBr_6]^{4-}$octahedra increases significantly from C6BrN2 to C7BrN2 while there is a small decrease from C7BrN2 to C8BrN2 (Figure 6C). Looking into the bond angle variance of the studied lead bromide materials alongside their lead iodide analogues, there is an apparent trend as seen from Figures 6D that C6IN2 and C8IN2 have consistently larger distortions of the individual $[PbI_6]^{4-}$ octahedra in comparison to C6BrN2 and C8BrN2 respectively. This is readily observable by comparing side-to-side the crystal structure representations (Figure 4). In respect to the bond length distortion (calculated from the formula $\Delta d = \left(\frac{1}{6}\right) \sum_{i=6}^{6} \left[\frac{d_n^2 - d}{d}\right]$) of the individual $[PbBr_6]^{4-}$ octahedra, it

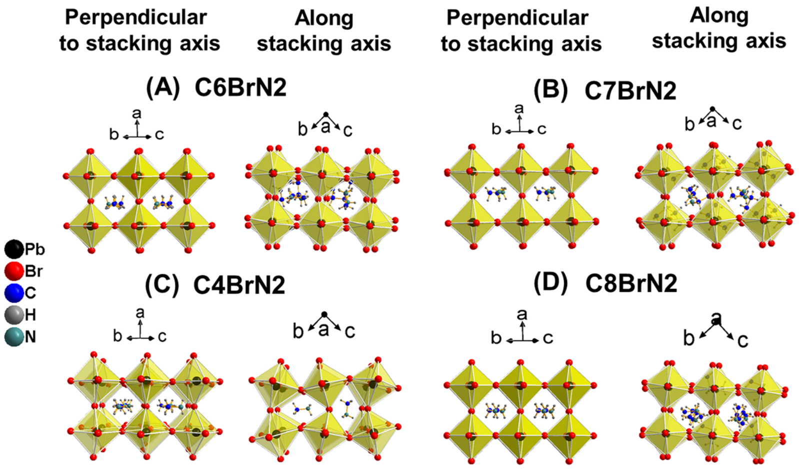

Figure 5. Side-view and top-down view of the single-crystal structures of (**A**) C6BrN2, (**B**) C7BrN2, (**C**) C4BrN2, and (**D**) C8BrN2.

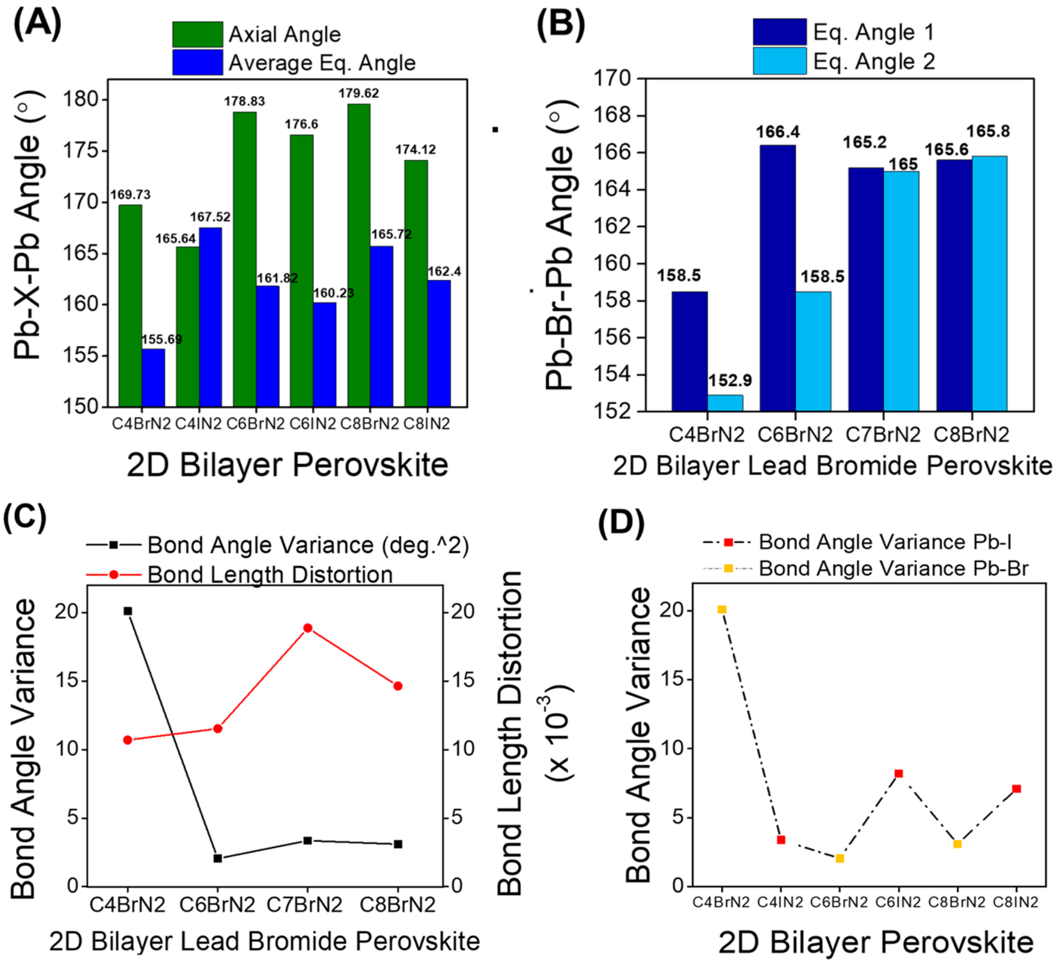

Figure 6. (**A**) Average axial and equatorial Pb−Br−Pb angles, (**B**) equatorial Pb−Br−Pb angles, and (**C**) bond angle variance and bond length distortion of C4BrN2, C6BrN2, C7BrN2, and C8BrN2. (**D**) Bond angle variance of C4BrN2, C6BrN2, and C8BrN2 versus C4IN2, C6IN2, and C8IN2.

appears from Figure S10 that both C8BrN2 and C8IN2 have larger bond length distortion values than their C6 analogues. Another trend seems to start from the higher symmetry orthorhombic C4BrN2, which has smaller octahedral bond length distortion and extends to the monoclinic C6BrN2 and C8BrN2, where the bond distortion increases consecutively (Figure S10).

Optoelectronic Properties. The bandgap of the synthesized compounds was measured by diffuse reflectance spectroscopy of powder samples, where the Kubelka−Munk model was used to derive the absorption.[136] The bandgap of hybrid lead bromide perovskites is larger than their lead iodide analogues. This is mostly the result of the increased electronegativity of Br (versus I) which comparatively lowers the energy of the valence band maximum, consisting of antibonding hybridization between the 4p orbitals of Br and 6s orbitals of Pb, while the conduction band minimum is left mostly unchanged (which consists of bonding hybridization between 6p orbitals of Pb). Previously, the narrow PL emission of layered lead bromide perovskite films has been tuned across the UV visible region based on *n*-layer thickness, where $n = 1$ members can generate blue-light emission[115,122,137] and $n \geqslant 2$ can generate green-light emission.[111−115,117,138,139]

The bandgaps of the 2D perovskites are blue-shifted in comparison to the bandgap of $MAPbBr_3$ (~2.21 eV) because of the strong quantum confinement in the thinner perovskite layers.[24,25,140] The UV absorption spectra are typical of layered perovskites, which present two characteristic features: an absorption edge and an excitonic peak below the bandgap (Table 2). The bandgap is estimated by extrapolating a line from the absorption peak toward the *x* axis. Figure 7A displays the absorption spectra which exhibit the characteristic absorption edge: 2.68 eV for C4BrN2, 2.70 eV for C7BrN2, 2.71 eV for C8BrN2, and 2.74 eV for C6BrN2. As seen in Figure 7B, the 2D bilayer perovskites display strong PL

Table 2. Experimentally Measured Bandgap Energy (eV) from the Absorption Spectra and Corresponding PL Peak Positions (eV) for Bulk Crystalline Powders of $(C_mH_{2m+1}NH_3)_2(CH_3NH_3)Pb_2X_7$ (X = Br, I; *m* = 4, 6−8)

bilayer lead halide perovskite	bandgap (abs. edge)	PL emission (exciton peak)	average lifetime
C4BrN2	2.68 eV	2.42 eV	3.91 ns
C4IN2	2.17 eV[10]	2.12 eV[10]	223.52 ps[50]
C6BrN2	2.74 eV	2.58 eV	6.16 ns
C6IN2	2.10 eV[34]	2.14 eV[34]	303 ps[34]
C7BrN2	2.70 eV	2.52 eV	1.27 ns
C8BrN2	2.71 eV	2.49 eV	0.44 ns
C8IN2	2.16 eV	2.15 eV	-

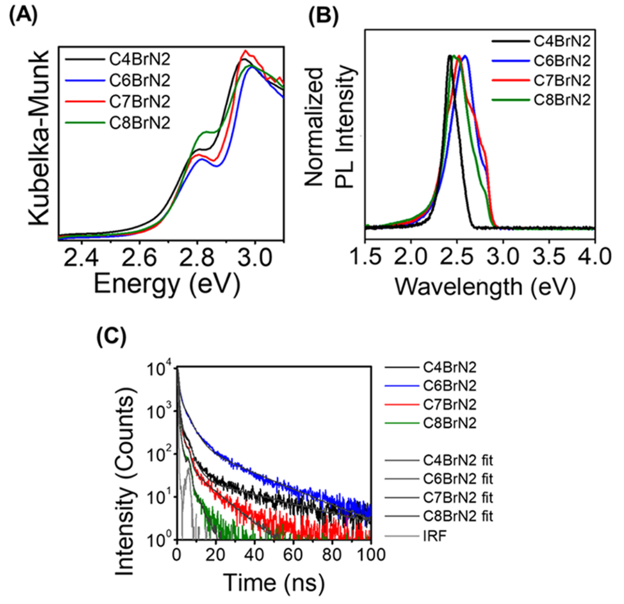

Figure 7. (**A**) Optical absorption spectra, (**B**) steady-state PL emission spectra collected with a long pass filter of 370 nm and excited at 405 nm, and (**C**) time-resolved PL decays and fitting collected at room temperature of C4BrN2, C6BrN2, C7BrN2, and C8BrN2.

emission at room temperature due to the presence of stable excitons at room temperature, with an emission energy close to the energy value of the excitonic peak in the absorption spectra.[10] The PL emission peak of C4BrN2 is 512 nm = 2.42 eV, C6BrN2 is 480 nm = 2.58 eV, C7BrN2 is 493 nm = 2.52 eV, and C8BrN2 is 499 nm = 2.49 eV. These values match closely to the exciton peak positions of the corresponding absorption spectra. Therefore, the organic spacer influences the luminescent properties of the materials mainly through its templating within the inorganic framework and the resulting distortions in the perovskite Pb−Br−Pb bridging angles.[141] Lastly, it is worth noting that the asymmetric shape of the PL emission peak in the compounds reported here, as well as other reported 2D bromide perovskites which requires additional exploration, beyond the scope of this current work.[81,103]

The dynamics of photoexcited carriers in multilayer 2D lead bromide crystals have not been studied systematically, and to date, a study correlating structure and carrier dynamics has not been reported. Recently a study investigated the correlation of dielectric confinement and exciton binding energy between 3D and 2D monolayer ($n = 1$) perovskites by varying the halide ion.[142] To gain a deeper understanding of the lifetime of the excitons in the studied bilayer 2D materials, time-resolved PL measurements were conducted (see the SI for details). Time-resolved PL measurements at room temperature reveal that the average lifetime in the family of bilayer materials decreases from C6BrN2 to C8BrN2. C6BrN2 exhibits the longest lifetime of 6.16 ns, next is C4BrN2 with 3.91 ns, which is followed by C7BrN2 at 1.27 ns, and C8BrN2 has the shortest lifetime of 0.42 ns (Figure 7C). These photoexcited carrier decay times are substantially longer compared to the 2D lead iodide analogues.[27,28,34] Specifically, the corresponding bilayer C6IN2 has an average lifetime of 303 ps versus that of C6BrN2 with 6.16 ns, reported here.[34] Based on the literature, others have provided significantly longer carrier lifetime values of the reported multilayer lead bromide perovskites consistently, in comparison to lead iodide perovskites, though development and analysis of this phenomenon has not been elaborated yet.[81,85,91,94−98,101−103] An initial interpretation for this interesting difference is developed further below (Theory and Electronic Structure Calculations).

Thermal Properties. A common phenomenon in hybrid halide perovskites is temperature-dependent phase transitions associated with the flexible and dynamic nature of the organic cations. Phase transitions are usually accompanied by changes in the structural configuration of the compound and thermal capacity; however, in 2D hybrid halide perovskites these do not cause dramatic structural changes but rather adjustments in the crystal packing that result in space group changes.[36,38] To study the phase transitions in the titled materials, differential scanning calorimetry (DSC) measurements were performed along with variable-temperature PXRD (VT-PXRD) and SCXRD at different temperatures. Reversible-cycle DSC measurements were performed in the temperature range of −50 to 220 °C. From the DSC measurements it was possible to identify the phase transition temperatures for each compound; all are reversible according to the DSC heating and cooling cycle (Figure S14). The sharp shape of the transition peaks presents the characteristic of a first-order transition. Specifically, C6BrN2 has two endothermic peaks at −25 and 33 °C with no other peaks apparent in the temperature range scanned (−50 to 220 °C) (Figure S14A). Likewise, in the same range C7BrN2 has one endothermic peak at around −13 °C while C8BrN2 has two endothermic peaks at around −12 °C and around 2 °C (Figure S14B, C). In all three compounds, the values of the enthalpies of the endotherms on the reversible heating cycle are slightly higher.

Additionally, to gain deeper structural insight from the phase transitions, VT-PXRD was carried out on the C6BrN2 sample (Figure S12). Upon the heating cycle from 20 to 80 °C, the reflections shift toward lower 2θ values in the recorded PXRD pattern, beginning at 30 °C in good correspondence with the DSC measurements (Figure S14A). This phase transition near room temperature justifies the difficulty of obtaining the precise single-crystal structure of C6BrN2 at room temperature because of the additional disorder and possible phase coexistence caused from its inherent phase transition behavior. The phase transitions are fully reversible in the examined heating temperature range, where the initial and final diffraction patterns match precisely (Figure S13).

The crystal structure of C6BrN2 at high temperature (HT) 50 °C was solved in the centrosymmetric space group $C2/c$ with $R_{\mathrm{obs}} = 8.66\%$ (Table S6) supported by the Hamilton test. Above a room-temperature phase transition, the stacking axis is elongated by 2.49 Å. The average Pb−Br bond length in the inorganic octahedra remains near 2.97 Å as in the room-temperature phase, reflecting no additional distortions associated with the phase transition at 50 °C. A VT-PXRD cooling cycle was carried out on the C6BrN2 sample in the temperature range of from 20 °C to −100 °C (Figure S12B). The Bragg reflections shift to higher 2θ, where the below room-temperature transition −30 °C is apparent, confirming the DSC data. At −40 to −70 °C, there is a splitting of the lowest basal reflection, which suggests the basal plane is lowering in symmetry. Again, the phase transitions are fully reversible in the examined cooling temperature range, where the initial and final diffraction patterns match exactly (Figure S13). The consequences in terms of nature and symmetry of the phase transition order parameter are explored in the theoretical part (vide infra).

Thermogravimetric analysis (TGA) measurements were conducted on C6BrN2, C7BrN2, and C8BrN2 to gain information on the thermal stability of the new materials (Figure S15−S17). All three materials are thermally stable up to 293 °C, whereas there are two distinct decompositions steps following at around 260 and 460 °C (Figure S15−S17). The first weight loss at around 260 °C corresponds to the decomposition of the organic components of the structure and HBr. The following weight loss in the second step corresponds to the decomposition of the inorganic component $[PbBr_6]^{4-}$, above its melting temperature.[92] The thermal data of the bilayer lead bromide perovskites' crystal powders demonstrates similar temperatures of decomposition their reported lead iodide analogues.[34]

Theory and Electronic Structure Calculations. It is indeed interesting to perform a symmetry analysis of the relation between the *Cc* and *C*2/*c* space groups obtained for the low and high temperature phases of C6BrN2. The simultaneous losses of the high temperature inversion symmetry and binary axis along *b* allows to predict that the associated ferroelectric phase transition corresponds to the creation of a permanent dipole in the (*a*, *c*) plane. Using Landau theory, the permanent dipole is defined as the phase transition order parameter related to the $\Gamma_2^-(B_u)$ irreducible representation of the parent *C*2/*c* (C_{2h}) space (point) group at the Γ point of the Brillouin zone. The electronic structure of C6BrN2 has been computed using density functional theory (DFT, see the SI) and the permanent dipole per unit cell was calculated using the geometric Berry phase approach.[143] In this DFT-based approach for periodic systems, the polarization of the nonpolar phase is taken as a reference.[144] Starting from the centrosymmetric *C*2/*c* with a polarization set to zero, the numerical computation predicts that the polarization along the stacking axis *a* shall be orders of magnitude larger than that along the in-plane axis *c* (Figure S18).

The electronic band structures of the newly reported materials C6BrN2, C7BrN2, and C8BrN2 were theoretically calculated. All three compounds show a nearly direct bandgap at the Γ point of the Brillouin zone (Figure 8A, C, E), similar to that of reported 2D hybrid lead iodide RP perovskites.[10] The electronic bands are dispersive within the layers due to the corner-sharing connectivity of the $[PbBr_6]^{4-}$ octahedra. The bands demonstrate flat dispersion across the layers in the stacking direction, which is caused by the structural discontinuity of the organic spacers. All structures assigned to a noncentrosymmetric group show small band splitting at the valence band maximum and conduction band minimum. This feature is a signature of the Rashba coupling caused by the presence of large spin−orbit coupling and crystal polarity that has been previously described in lead-based halide perovskites.[145] The computed bandgaps for C6BrN2, C7BrN2, and C8BrN2 are 1.54, 1.46, and 1.50 eV, respectively (Table 3), in agreement with the experimental trend, despite the well-known DFT underestimation of bandgaps. Interestingly, this trend is recovered in the calculations only when the *Cc* structure is considered for C6BrN2. Indeed, the *C*2/*c* centrosymmetric structure leads to a bandgap of 1.60 eV, larger than C7BrN2 and C8BrN2 (Figure S19 and Table 3). This supports the assignment of the C6BrN2 structure as non-centrosymmetric at room temperature.

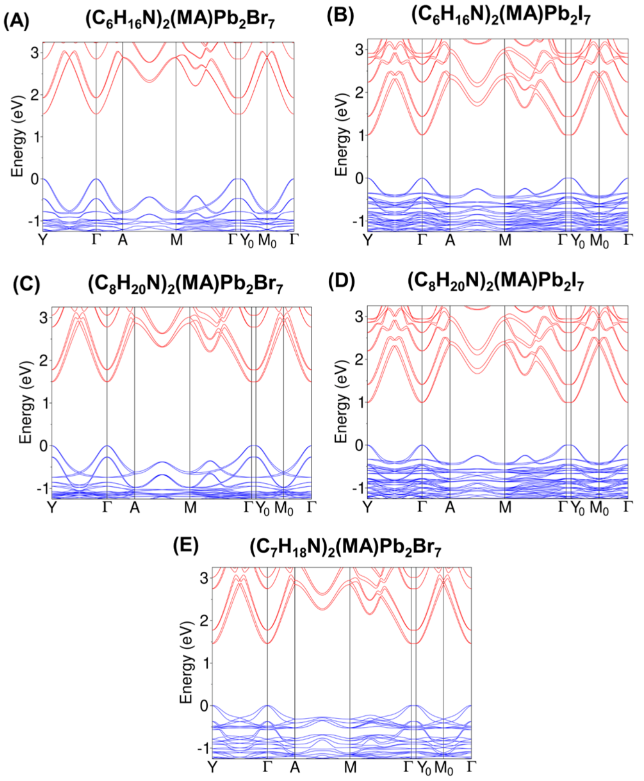

Figure 8. DFT computed band structures of (**A**) C6BrN2, (**B**) C6IN2, (**C**) C8BrN2, (**D**) C8IN2, and (**E**) C7BrN2. The valence and conduction bands are depicted in blue and red, respectively. All compounds exhibit strong dispersion within the layers and flat dispersion in the stacking direction.

The methodic study of the bilayer lead bromide perovskites in bulk provides a good opportunity to examine for the first time, the differences associated with exchanging the halide ion from iodide to bromide on the electronic structure and its experimental expression in layered perovskites' optoelectronic properties. Specifically, based on the significantly longer PL lifetime of the bromide analogues reported here, we inspect first the band dispersion and effective mass in the in-plane direction to gain insight on the radiative electronic transitions. For this reason, we compare the electronic structures of C6BrN2 versus C6IN2 and C8BrN2 versus C8IN2. The iodide compounds show similar band structures with very dispersive bands in the corner-sharing directions that become flat in the stacking direction (Figure 8A−D). As expected, the bandgaps are smaller than for the bromide compounds. Interestingly, the size of the cation chain seems to have nearly no effect on the bandgap of the lead iodide analogues that remains around 1.00 eV (1.00 eV for C6IN2 and C8IN2 for 0.99 eV; see Figure 8). When computing the effective masses along the layer direction for all bromide and iodide compounds, one can see a continuous decrease when going from C6BrN2 ($\mu = 0.075m_0$) to C8BrN2 ($\mu = 0.064m_0$), as seen in Figure 9A and Table 3. Meanwhile, the reduced effective mass slightly increases from C6IN2 ($\mu = 0.057m_0$) to C8IN2 ($\mu = 0.061m_0$) but remains smaller than in the corresponding bromide structures (Table 3). Recently, a study reported the tailorable relationship between the carrier effective masses in 2D halide perovksites with the choice of organic spacer and metal cation, confirming how the effective mass can be broadly tuned through ionic composition.[146]

Table 3. Computed Bandgaps (E_G), Hole (m_h), Electron (m_e), and Reduced Effective Masses (μ) for C6BrN2, C7BrN2, C8BrN2, C6IN2, and C8IN2 Compounds[a]

bilayer lead bromide perovskite	C6BrN2 H.T. (C2/*c*)	C6BrN2 (C2/*c*)	C6BrN2 (*Cc*)	C7BrN2 (*Cc*)	C8BrN2 (*Cc*)
E_G (eV)	1.52	1.60	1.54	1.46	1.50
m_h (m_0)	−0.134	−0.156	−0.171	−0.140	−0.137
m_e (m_0)	0.128	0.142	0.135	0.121	0.122
μ (m_0)	0.065	0.074	0.075	0.065	0.064
bilayer lead iodide perovskite		C6IN2 (*Cc*)			C8IN2 (*Cc*)
E_G (eV)		1.01			0.99
m_h (m_0)		−0.128			−0.142
m_e (m_0)		0.102			0.107
μ (m_0)		0.057			0.061

[a] In addition to the noncentrosymmetric *Cc* structure of C6BrN2, the computed bandgaps and reduced effective masses of the noncentrosymmetric C2/*c* and HT phase at 323 K structures are given.

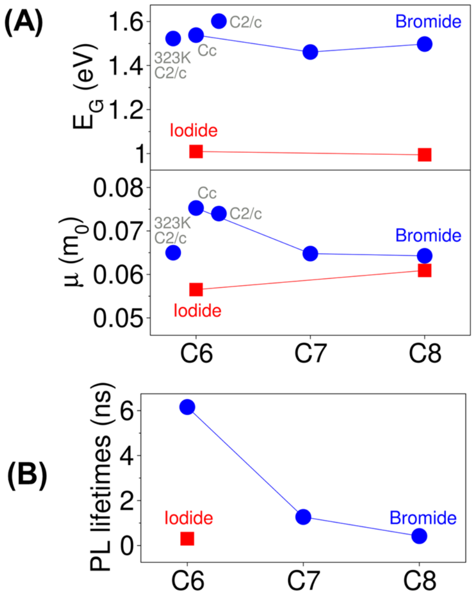

Figure 9. (**A**) Computed bandgaps (E_G) and reduced effective masses (μ) for C6BrN2, C7BrN2, and C8BrN2 (blue circles), as well as C6IN2 and C8IN2 (red squares) compounds. In addition to the noncentrosymmetric *Cc* structure of C6BrN2, the computed bandgaps of the noncentrosymmetric and the 323 K C2/*c* structures are given. (**B**) Measured photoluminescence lifetimes for C6BrN2, C7BrN2, C8BrN2 (blue circles), and C6IN2 (red square).

The spontaneous radiative lifetime is a complex quantity, especially when trying to account for additional strong excitonic effects, not affordable for such large structures from DFT calculations. It is nevertheless possible to discuss the observed experimental trends on the basis of classical dependence on the basic optoelectronic parameters.[147] The spontaneous radiative lifetime shall indeed exhibit a positive (negative) correlation with the effective mass (electronic band gap). The numerical trends for the spontaneous radiative lifetime are therefore in fair agreement with the measured PL lifetimes, but the observed differences may most likely result from variations of nonradiative recombinations. Indeed, detrimental nonradiative recombinations may result from charge localization effects and the coupling to low frequency structural density of states. These two aspects have been recently explored by nonadiabatic molecular dynamics in monolayer bromide compounds showing that lattice rigidity and a better lattice match between the perovskite layer and the organic barrier shall induce a reduction of nonradiative recombinations,[148] both aspects limiting the impact of the floppiness of the organic molecules. In addition, it has been shown experimentally that the softness of the organic barrier is correlated to an enhancement of the electron−phonon coupling processes, promoting the capture of carriers by trap states.[122] Mechanical characterizations of layered iodide and bromide perovskites are scarce in the literature, but a complete comparative study of 3D hybrid perovskites' elastic constants clearly shows that the stiffness of the lattice is increased when going from iodine to bromide compounds.[149] A decrease of the out-plane stiffness as a function of the length of the alkyl chain was additionally observed for monolayered iodine perovskites.[126] Therefore, an increase of the alkyl chain length is expected to enhance nonradiative recombinations, which is consistent with the decrease of the PL lifetime with the increase in chain length observed in the present work.

Next, in order to gauge comparatively strain effects between iodide and bromide compounds, it is enlightening to introduce the concept of lattice mismatch.[125] Predicting the relative stability and strain accumulation at room temperature in layered perovskites is currently beyond the reach of atomistic simulations, essentially due to the importance of the entropy contributions related to phonons and the unusual lattice anharmonicity. It is nevertheless possible to adopt a semi-empirical and elasticity-based approach that has been successfully used for decades for classical semiconductor heterostructures. Within this framework, the strain accumulation is analyzed in multilayered ($n > 1$) perovskites, considering them as layered composites of the related monolayered ($n = 1$) and bulk compounds ($n = \infty$). It is therefore important to have the smallest possible lattice mismatch between these two reference compounds in order to minimize strain accumulation at intermediate compositions ($1 < n < \infty$).[125] Interestingly, this can lead to purely qualitative empirical prediction, relying only on available experimental data at RT for $n = 1$ and ∞. The computed in-plane average lattice strains are reported in Figure 10, considering the room temperature experimental data for $n = 1$ compounds as the reference for strain computation, and the dashed lines define the maximum strain values obtained for the related 3D compounds.[125] The experimental lattice mismatch with the related 3D perovskite $MAPbBr_3$ is sizably smaller for the C4BrN2 layered perovskite, in contrast to its lead iodide analogues. The enhanced rigidity of the bromide compounds in comparison to the iodide analogues, which is beneficial in limiting nonradiative recombinations, shall in turn limit the

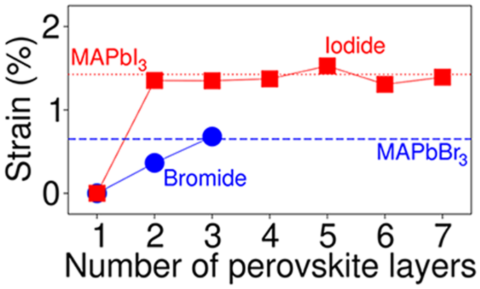

Figure 10. In-plane average lattice strain considering the monolayered compounds with C4 spacer as references for bromide (blue circles) and iodide (red squares) compounds. The dashed blue and dotted red lines represent the lattice mismatches with the related $MAPbBr_3$ and $MAPbI_3$ compounds, respectively.

possibility of growth of multilayer perovskites.[125] However, this detrimental effect is compensated by a reduced lattice mismatch in the bromide composites analyzed in the present study, by comparison to iodide ones. A summative perspective on the structure−property relationship in 2D hybrid halide perovskites is illustrated in Table 4.

Film Assembly. The majority of 2D perovskite films reported employ solutions made from mixtures of the precursor components (e.g., PbI_2, $PbBr_2$, MAI, MABr, etc.) that are casted on substrates.[30,33,35,111−114,117,138,150,151] Herein, instead the method of film fabrication for all studied compounds was to dissolve the corresponding crystals in anhydrous DMF solvent. Film fabrication of the studied materials (C4BrN2,C6BrN2, C7BrN2, and C8BrN2) was undertaken using both the one-step and hot-casting deposition methods. Details of the film assembly are in the experimental section (see the SI). In brief, the one-step method consists of spin-coating the perovskite solution onto the substrate, followed by thermal annealing on a hot plate at 110 °C. Differently, for the so-called hot-casting method, the substrate is heated on a hot plate at 110 °C prior to spin-coating the perovskite solution.[19]

The orientation of layered perovskites on the substrates (referring to inorganic layers parallel, perpendicular, or a mixture of the two), needs to be a premier area of focus for the study and development of such materials for high performance LED devices.[117,119,152] Thus, far, there are few reports in the literature of consistent structural characterization accompanying characterization of optical properties, crystalline orientation, and device performance of multilayer lead bromide perovskite films, despite the commencing success of LEDs with bulk, lead bromide perovskites.[111−115,117,138,153,154] First, the case of parallel orientation of the inorganic layers to the substrate entails the conduction of charge carriers in the out-of-plane charge transport direction. As a result, this is linked to a less optimal device performance for certain photovoltaic and LED applications, but there are detectors where parallel orientation is preferred. Generally, parallel orientation is observed for thin films of low n members ($n < 3$) in the family of 2D lead iodide perovskites.[19] The relationship between n layer thickness and the corresponding behavior of crystalline orientation has not been investigated thoroughly for thin films of 2D multilayer lead bromide perovskites, hitherto. Second, the case of perpendicular orientation of the inorganic layers to the substrate allows charge carriers to travel through the conducting inorganic slabs between the electrodes. This is the optimal situation for the fabrication of efficient perovskite photovoltaic and LED devices. The hot-casting method has been shown to facilitate a preferable perpendicular orientation of perovskite films with high n members ($n > 3$) in the case of 2D lead iodide perovskites.[19,155]

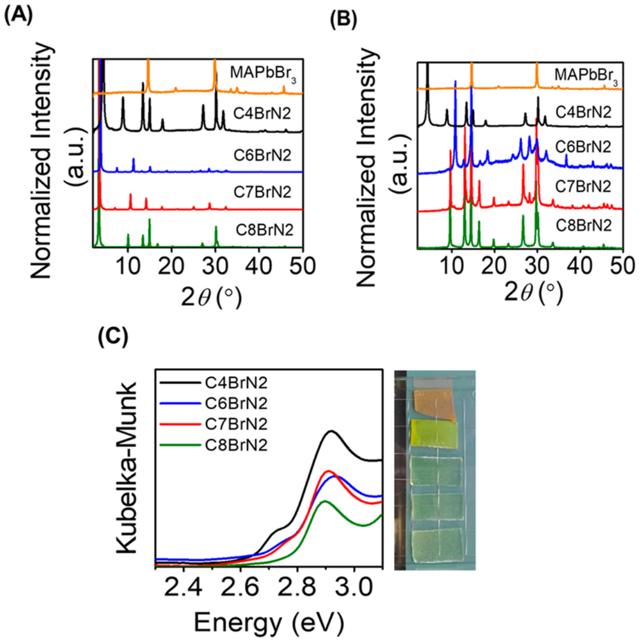

Figure 11. Powder X-ray diffraction patterns of thin-films of $MAPbBr_3$, C4BrN2, C6BrN2, C7BrN2, and C8BrN2 made from the (**A**) one-step and (**B**) hot-casting methods. (**C**) Absorption spectra of thin films C4BrN2, C6BrN2, C7BrN2, and C8BrN2 alongside picture of thin films.

Uniform phase films of $n = 2$ perovskites and $MAPbBr_3$ were fabricated outside the glovebox (16% relative humidity) with the one-step method, which exhibit two low-angle basal Bragg peaks below $\sim 2\theta = 13°$ as seen from the PXRD patterns (Figure 11A). The presence of these low-angle peaks in the films indicates a parallel orientation of the inorganic perovskite layers to the substrate. Contrarily, the hot-casting method produced films with different PXRD patterns (Figure 11B). As mentioned, the same solution concentrations were used for both film deposition methods. The PXRD patterns of the thin films produced from the hot-casting method do not show the low-angle reflections (below $\sim 2\theta = 10°$) present for the bilayer perovskites with long-chain monoamines C6BrN2, C7BrN2,

Table 4. Summative Perspective on the Structure−Property Relationship in 2D Hybrid Halide Perovskites

bilayer lead halide perovskite	tuned parameter	lattice match and rigidity	lattice strain	nonradiative recombination	carrier lifetime (T)	film stability
$(C_mH_{2m}N)_2(MA)Pb_2X_7$	m = chain length of monoamine; m↑	↓	-	↑	↓	↑
	electronegative halide X^- (from Br^- to I^-)	↓	↑	↑	↓	↓

and C8BrN2, while, for the C4BrN2 films, the low-angle reflections are present (Figure 11B). The optical absorption spectra of the films fabricated verify the phase composition of *n* = 2 perovskites (Figure 11C). The fact that orientation may be associated with the deposition method and/or organic spacer cation, as the PXRD patterns demonstrate the absence of low angle reflection peaks, is interesting. This seemed to be a consistent observation, after multiple trials of film fabrication with both deposition methods, outside the glovebox. As mentioned, the 2D bilayer lead iodide perovskite films present parallel orientation.[19,34] Multiple factors associated with the kinetics of lead bromide perovskites' nucleation and growth are suspected to be responsible for this indication of preferable crystalline orientation, including parameters such as humidity[156] and film-casting temperature[157] in ambient environment, as examined recently. Future comprehensive studies with GIWAXS (grazing-incidence wide-angle X-ray scattering) are required to answer definitively the unexplored questions of crystallinity and orientation in 2D multilayer lead bromide perovskites, which is outside the scope of the current study. Finally, fabrication of films in the nitrogen-filled glovebox improved the quality of film coverage by eye, in comparison to fabrication in ambient environment (Figure S29).

Film Stability Studies. We performed a comprehensive investigation of the stability of 2D hybrid lead bromide perovskite films, along with the comparison to the 3D $MAPbBr_3$. This information is critical to understand the environmental stability of the lead bromide analogues and to draw comparisons between the individual 2D members and 3D $MAPbBr_3$, as well as with the better-studied lead iodide analogues.[10,34] It is important to construe the origin of the stability of the studied 2D and 3D materials based on structural understanding in order to judiciously design and evaluate their performance in solar cells, LEDs, detectors, and lasing devices.[8−13,34,158−162]

A comprehensive set of stability studies were carried out for all studied materials ($MAPbBr_3$, C4BrN2, C6BrN2, C7BrN2, and C8BrN2) in the form of thin films without any encapsulation, examining the parameters of air, heat, and light stability. The films tested for stability were fabricated outside the glovebox, based on the hot-casting method. Regarding ambient air stability, the thin films of the studied materials were left in a drawer in an ambient environment (average 25 °C and 16% relative humidity) and in the dark for 5 months. All five materials show excellent stability for at least 5 months as witnessed from the PXRD pattern (Figures 12 and 13) and UV absorption spectra, which remain intact substantiating that the structural integrity and optical performance of the materials' thin films are maintained (Figure S21B). There was no change in the films' color nor formation of byproducts. This observation is especially interesting for the 3D $MAPbBr_3$ (Figure 12). In comparison, $MAPbI_3$ is much more unstable with rapid degradation in ambient air.[16] It has been reported that bromide substitution in $MAPbI_3$ films improves significantly the stability of the material under operating conditions, while offering high power conversion efficiency in solar cell devices.[158,163] Additionally, it has been proven that $MAPbBr_3$ films maintain their optical integrity after 120 h exposure to moisture.[159] We observe that $MAPbBr_3$ films exhibit exceptional stability to ambient moisture and air for an extended period of time. This superior stability of $MAPbBr_3$ is developed further below.

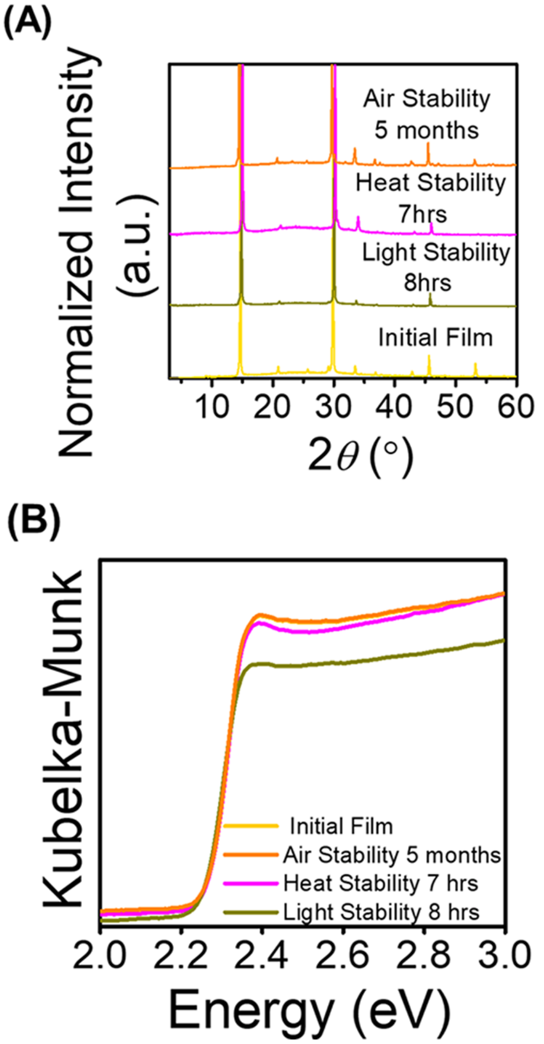

Figure 12. (**A**) Powder X-ray diffraction patterns and (**B**) absorption spectra of thin films of $MAPbBr_3$, before stability testing (yellow) and afterward from air stability testing after 5 months (orange), heat stability testing after 7 h total (pink), and light stability testing after 8 h total (green).

Next, the extrinsic light stability of all compounds was investigated by exposing unencapsulated films under light, 1 sun solar simulator (1000 W/m^2) for 4 and 8 h respectively, in ambient air condition with nominal/relative humidity 16%. In the first 4 h, C4BrN2 films had fully degraded as seen by the PXRD pattern (Figure 13A), where no Bragg reflections were visible while the absorption spectrum verified that the film had fully decomposed into $PbBr_2$ with a bandgap at 3.3 eV (Figure S22A). The C4BrN2 film turned from a bright yellow color to a colorless film. In contrast, the $MAPbBr_3$, C6BrN2, and C7BrN2 films and C8BrN2 remained stable and maintained their optical properties, as there was no impactful change in the PXRD pattern or the absorption spectra (Figures 12, 13, and S22A). After 8 h in total light illumination of 1 sun intensity, the PXRD patterns corroborate the stability $MAPbBr_3$, C6BrN2, C7BrN2, and C8BrN2 with their diffraction peaks remaining mostly unchanged (Figures 12 and 13).

The films' color was maintained for $MAPbBr_3$, C7BrN2, and C8BrN2 but with duller quality, while the C6BrN2 film had a very light-yellow color. However, the optical absorption spectra demonstrated a more accurate perception of the stability. The

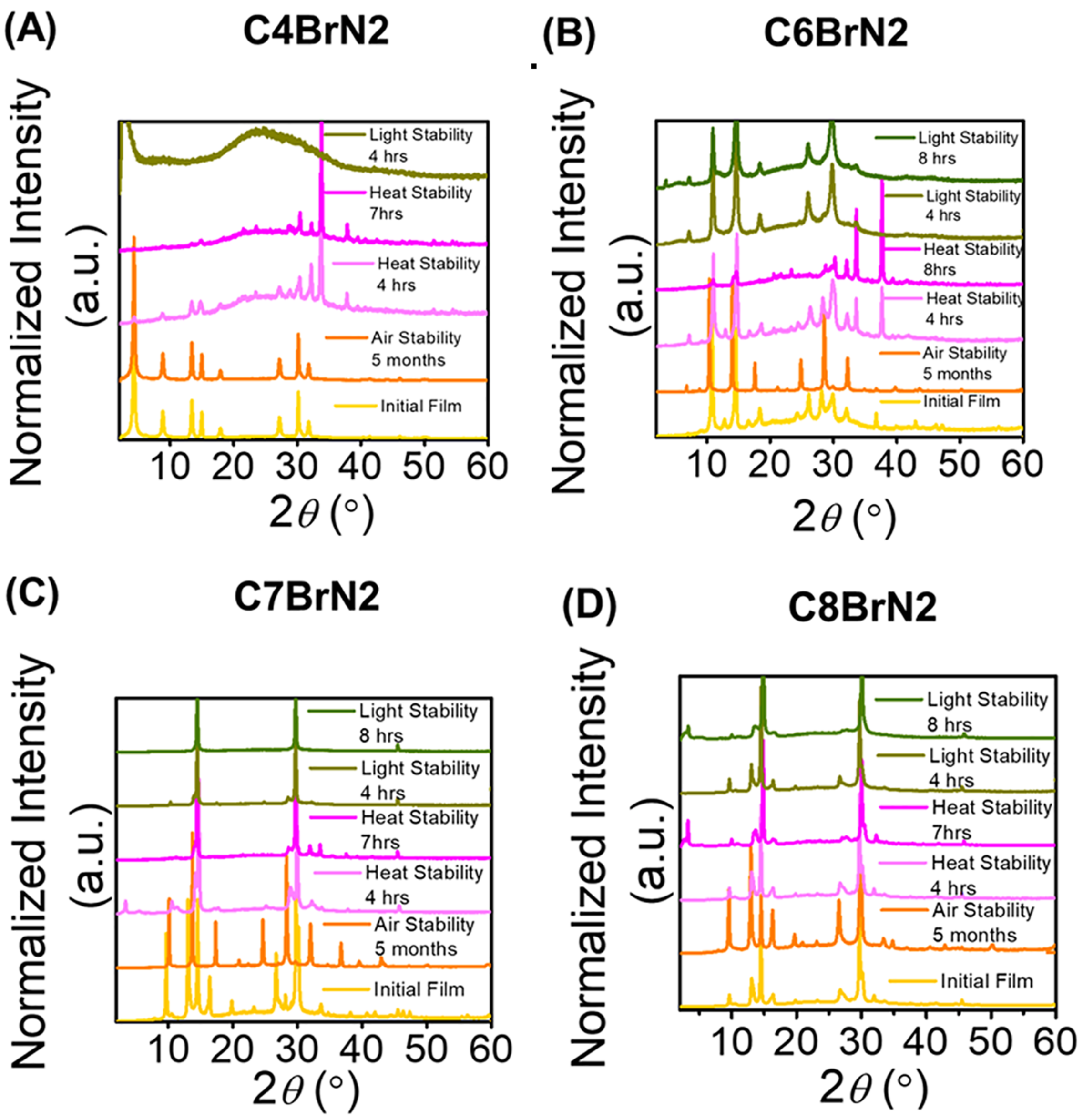

Figure 13. Powder X-ray diffraction patterns in ambient conditions, from before and after stability tests for unencapsulated thins films of (**A**) C4BrN2, (**B**) C6BrN2, (**C**) C7BrN2, and (**D**) C8BrN2. Color code: before stability test initial films (yellow), air stability testing after 5 months (orange), heat stability testing 4 and 7 h total (pink), and light stability testing 4 and 8 h (green).

C6BrN2 film has decomposed into $PbBr_2$ (bandgap at 3.3 eV) and $MAPbBr_3$ (bandgap at 2.2 eV) (Figure S22B). The optical absorption spectra suggest that $MAPbBr_3$, C7BrN2, and C8BrN2 films were still stable, although C7BrN2 and C8BrN2 films developed an absorption edge at 2.2 eV, corresponding to $MAPbBr_3$, which C7BrN2 and C8BrN2 were partly and slowly degrading into (Figure S22B). Therefore, the traces of byproducts being formed can be detected by optical absorption spectroscopy, emphasizing the need to monitor both the structural and optical integrity of the materials during stability tests. Remarkably, $MAPbBr_3$, and in sharp contrast to what is known for $MAPbI_3$, remained intact as seen from the PXRD pattern and absorption spectra. This film maintained its orange color but was slightly duller than in the beginning of the testing (Figure 12). In sum, under a light of 1 sun in ambient conditions, (i) the C4BrN2 film was only stable for up to 4 h, (ii) the C6BrN2 film was structurally stable up to 8 h and optically stable up to 4 h, (iii) C7BrN2 and C8BrN2 films were structurally and optically stable up to 8 h, and (iv) $MAPbBr_3$ films were structurally and optically stable for at least 8 h. The stability of $MAPbBr_3$ is consistent with previous reports[159,164] where $MAPbBr_3$ films maintain their optical integrity after 130 h exposure to light under dry air. Our studies indicate that the inherent light stability of $MAPbBr_3$ can be coupled to its enhanced moisture stability, mentioned above.

Finally, the thermal stability of unencapsulated $MAPbBr_3$, C4BrN2, C6BrN2, C7BrN2, and C8BrN2 films was tested on hot plates at 100 °C in air under ambient light from 4 h up to 7 h, constantly. For the first 4 h, $MAPbBr_3$, C6BrN2, C7BrN2, and C8BrN2 films did not show significant decomposition as the PXRD patterns were relatively similar to the initial PXRD pattern of the films, before being treated to heat (Figure 13). Specifically, the C4BrN2 film presented a visual decolorization toward a yellow−white color, yet the PXRD pattern maintained the characteristic low-angle peaks but with significantly lower crystallinity (Figure 13). Concurrently, the C6BrN2 film showed lower crystallinity than initially, witnessed by the signal-to-noise ratio in the PXRD pattern. The PXRD pattern of C7BrN2 displayed the characteristic low-angle peaks for $2\theta < 13°$, indicating possible change of orientation (likewise observed after treatment to light, mentioned above, Figure 13). We have observed previously this change of behavior of crystal orientation in the heat and light treatment of 2D lead iodide perovskite films.[34] Recently, the crystallographic reorientation in polycrystalline 3D perovskite films was demonstrated to be induced by moisture exposure, which also revealed a relationship to the amount of organic cation present on the films' surface.[156] Further examination of the crystallization reorientation in 2D perovskite films can provide an impactful parameter to control for optimal device performance over extended periods of time.

After the 4 h of heat treatment, the optical absorption spectra of the films were collected (Figure S24A). The optical absorption spectra agree with the PXRD pattern clearly affirming that the $MAPbBr_3$, C6BrN2, C7BrN2, and C8BrN2 films maintained their optical properties, as well as structural integrity during the first 4 h of heat treatment. The C4BrN2 film showed multiple peaks in the absorption spectra: 2.2, 2.65, and 3.3 eV, corresponding to the formation of a small amount of $MAPbBr_3$ (2.2 eV) and formation of $PbBr_2$ (3.3 eV) as a major product which was reflected from the decolorization of the films toward a white color (Figure S24A). Next, PXRD patterns of the studied films were collected after 5 h in total of heat treatment (Figure S25B). The C4BrN2 films showed full decolorization from yellow to white, accompanied by the disappearance of the characteristic peaks in the PXRD pattern that showed highly amorphous character. The $MAPbBr_3$, C6BrN2, C7BrN2, and C8BrN2 films demonstrated no significant change based on PXRD. Lastly, the remaining $MAPbBr_3$, C6BrN2, C7BrN2, and C8BrN2 films were examined after 7 h in total of heat treatment. Impressively, the PXRD pattern for $MAPbBr_3$ did not denote significant changes (Figure 12A). The PXRD pattern of the C6BrN2 film maintained the characteristic low angle peaks but the crystalline quality had deteriorated (Figure 13B). The C7BrN2 film's low-angle peaks were not present anymore in the PXRD pattern, while, in contrast, the C8BrN2 film's PXRD pattern demonstrated the existence of its low-angle basal reflections. The absorption spectra indicate partial decomposition of C6BrN2 film to $PbBr_2$ whose bandgap is at 3.3 eV (Figure S24B). The optical spectra of C7BrN2 and C8BrN2 films confirmed also their partial decomposition with absorption edges at 2.2 ($MAPbBr_3$ phase), 3.3 ($PbBr_2$ phase), and the formation of higher $n = 3$ layers, with an absorption peak at 2.6 eV (Figure S24B). The optical properties of $MAPbBr_3$ were maintained (Figure 12B). To summarize, under heat treatment of 100 °C (as indicated on hot plate) in ambient air and light, (i) the C4BrN2 film was stable up to 4 h, (ii) the C6BrN2 film was stable up to 5 h, (iii) C7Br and C8Br were stable up to 7 h, and (iv) $MAPbBr_3$ was stable for at least 7 h. Thus, there is an overall trend in the stability of bilayer lead bromide perovskites, where increasing the length of the carbon chain in the organic spacer cation leads to greater stability of the corresponding perovskite. This seems to be due to the sequential increase in hydrophobicity of the organic spacer cation. $MAPbBr_3$ manifests superior stability of over 7 h, maintaining its structural and optical properties.

Consequently, $MAPbBr_3$ has superior stability in comparison with $MAPbI_3$, which starts to decompose into PbI_2 within 4 h of heating in the same testing conditions.[34] The superior thermal stability of $MAPbBr_3$ over $MAPbI_3$ films is demonstrated experimentally. This behavior of greater air, light, and heat stability of $MAPbBr_3$ over $MAPbI_3$ has been alluded to before based on the published work regarding $MAPbBr_3$ films' and devices' moisture−light stability, and our present work validates these findings.[159,160,164] The overall greater stability performance of $MAPbBr_3$ can be reasoned based on the structural and thermodynamic argument that $MAPbBr_3$ has a smaller lattice than $MAPbI_3$. This means that $MAPbBr_3$ has a higher Madelung lattice energy, thus decomposition is more difficult than in $MAPbI_3$. These observations are supported by the values of the formation enthalpy which are more endothermic for $MAPbI_3$ ($\Delta H_f = 34.50 \pm 1.01$ kJ/mol) than $MAPbBr_3$ ($\Delta H_f = 6.69 \pm 1.41$ kJ/mol).[165]

In both heat and light exposure under ambient conditions, $MAPbBr_3$ manifests superior stability over the 2D bilayer bromide perovskites. In the case of hybrid lead iodide perovskites, however, the 2D congeners exhibit greater stability over the 3D $MAPbI_3$, which is considerably less stable in air and under operating conditions. In this study, we can therefore conclude that the 2D and 3D hybrid lead bromide perovskites have overall greater extrinsic stability under operating conditions than the 2D and 3D hybrid lead iodide perovskites. We previously reported that the bilayer C6IN2 under the same conditions of heat 100 °C (on hot plate) decomposes immediately and under exposure to light 1 sun showed structural stability up to 10 h, as judged only by PXRD.[34] Thus, the C6BrN2 has considerably improved structural and optical stability comparatively over C6IN2. The superior environmental stability of the $n = 2$ lead bromide perovskites and excellent optoelectronic properties renders the family very attractive for light emission applications. It should be noted that these operating tests are a reliable evaluation of the materials' stability under the unoptimized laboratory conditions and as such can be further optimized for dedicated device work, as preliminary work has shown.[114]

Switching Spectroscopy-Piezoresponse Force Microscopy (SS-PFM). Ferroelectricity has been reported in several hybrid, layered lead bromide and monolayer lead chloride perovskites, such as with C4BrN2, where the ferroelectric reversal polarization behavior is noted as evidence of this property, along with the noncentrosymmetric crystal structure and Curie temperature phase transition.[68,69,74,166,31,91,94,95,97,98,104−107] For 2D perovskites, the structural origin of the recorded ferroelectric spontaneous polarization is reported to be associated with the orientation of the C−N bonds in the organic spacer molecules, with respect to the inorganic slab layers.[68,69] Specifically, the structures feature the C−N bonds of the ammonium cations aligning in the same direction that results in a net dipole. We proceeded to probe the existence of ferroelectric response in our titled materials by employing switching spectroscopy piezoresponse force microscopy (SS-PFM) measurements[68,69,74,107,166−169] at room temperature for thin films of the C6BrN2, C7BrN2, and C8BrN2 compounds.

Here, hot-casted thin film samples of each material were tested by SS-PFM where the inorganic slab (and thus the potential spontaneous polarization in question) can be better aligned perpendicular to the substrate surface and thus be

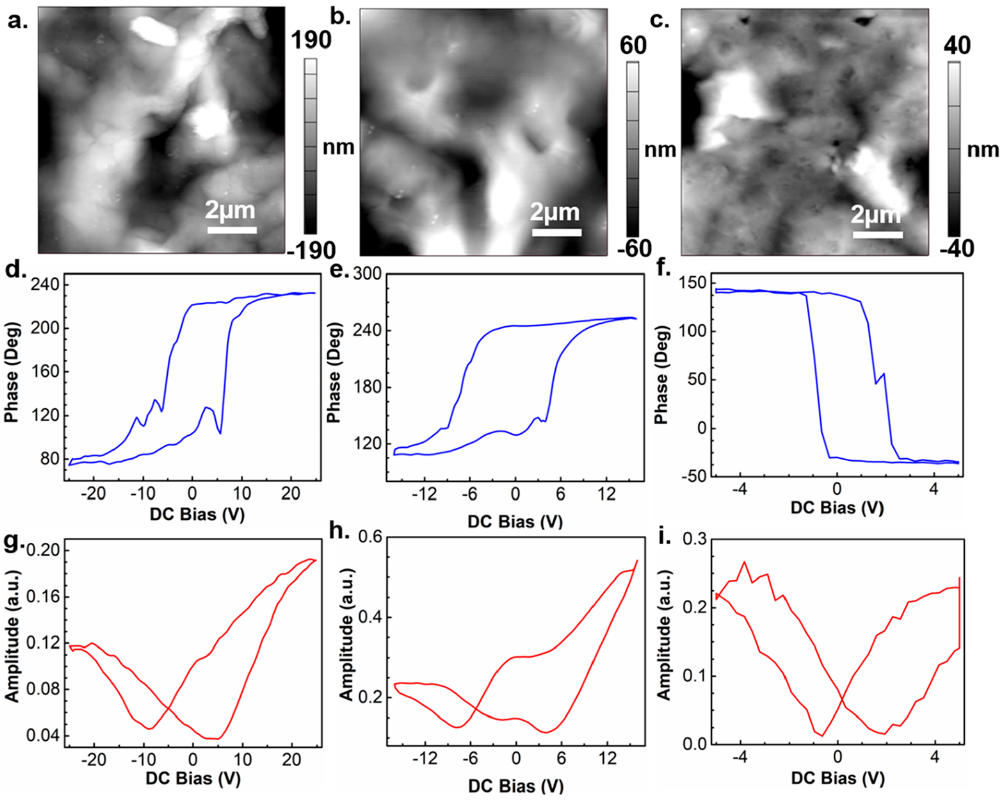

Figure 14. (**A**−**C**) Surface morphology of the resulting thin film samples of C6BrN2, C7BrN2, and C8BrN2. (**D**−**F**) Local response of the phase to the applied DC electrical field. (**G**−**I**) Local response of amplitude to the applied DC electrical field.

parallel to the applied electrical field through the AFM tip. Similar to the 2D halide perovskites reporting ferroelectricity in literature, the in-phase hysteresis loop response and butterfly like feature in amplitude response, demonstrate a reversal polarization behavior in all the three materials described here (Figure 14).[68,69,74,107,166−171] For C6BrN2 the hysteresis loop and butterfly like amplitude response are below the Curie temperature found by DSC measurements, while this not the case for C7BrN2 and C8BrN2, alluding to the rare class of reorientated ferroelectrics where the paraelectric phase can belong to a polar point group accompanying the reorientation of the *P*−*E* hysteresis loop.[172]

Figure 14**A**−**C** shows the surface morphology of the thin film samples of C6BrN2, C7BrN2, and C8BrN2, respectively. Figure 14**D**−**F** and **G**−**I**, show the local response of the phase and amplitude to the applied DC polarization electrical field, respectively. We further investigated the replacement of the halide ions Br^- by I^- in C8BrN2 (Figure S26), where the ferroelectric response vanishes, which is in agreement with the trend found in $(C_6H_{11}NH_3)_2PbBr_{4-4x}I_{4x}$ ($C_6H_{11}NH_3$ = cyclohexylammonium and $0 \leqslant x \leqslant 1$).[69] Furthermore, we heated the C6BrN2 sample in situ to 40 °C, which is above the Curie temperature of this compound. The hysteresis loop and butterfly like amplitude response disappeared, suggesting a transition from ferroelectric state to nonferroelectric state at this temperature (Figure S27). Altogether, because of the presence of disorder in the organic layers in the studied materials, it is difficult to establish the origin of ferroelectricity on a single-crystal structural basis, as claimed in other 2D ferroelectric hybrid halide perovskites. Our SS-PFM measurements indicate ferroelectric response, providing new information on this property, but further data and analysis is needed, especially for single crystal samples for decisive structural conclusions regarding ferroelectricity in 2D hybrid lead halide perovskites.

■ CONCLUSIONS

The new members of the Ruddlesden−Popper phases with long organic spacers $(C_mH_{2m+1}NH_3)_2(CH_3NH_3)Pb_2Br_7$ (m = 6−8) reveal many unknown features about their structural parameters, stability, and photophysical properties. The aliphatic and long-chain monoammonium cations of hexylammonium (C6), heptylammonium (C7), and octylammonium (C8) are incorporated into the 2D halide perovskite network. A universal solution synthesis method for bulk, multilayer lead bromide perovskites is provided, initiating the expansion of this structural phase space. The decrease in the overall dimensions of the inorganic lattice in 2D lead bromide perovskites compared to the 2D lead iodide perovskites, leads to a greater lattice rigidity, along with smaller internal lattice strain. The lattice mismatch of the inorganic perovskite layer with the organic layer is magnified as the length of the monoammonium spacer cation increases. Additionally, the $(C_mH_{2m+1}NH_3)_2(CH_3NH_3)Pb_2Br_7$ (m = 6−8) perovskites present smaller distortion of the $[PbX_6]^{4-}$ octahedra, in comparison with their lead iodide congeners. The titled $n = 2$ lead bromide perovskites exhibit bandgap energies between 2.65−2.70 eV and display narrow-band emission due to the presence of stable excitons at room temperature. All four of the studied lead bromide perovskites (C4BrN2, C6BrN2, C7BrN2, and C8BrN2) demonstrate longer carrier lifetimes than those of the bulk, 2D lead iodide congeners. The generally longer lifetimes observed in the 2D lead bromide perovskites, compared to the lead iodides, could be because their lattice is more dynamic at room temperature as a result of the difference of the Pb−Br bonds with the Pb−I bonds. This nature of the lattice is indicated by the fact that the $n = 2$ lead bromide perovskites are more likely to violate the Goldschmidt tolerance factor and can accommodate larger spacers in their cages, in comparison to their lead iodide congeners. The dynamic disordering of the lattice on the electronic excitation time scale could cause delays in recombination. Thin film fabrication of the materials is realized through the straightforward processes of the hot-casting and one-step method, where comprehensive stability studies of the materials as thin films in ambient air, light, and heat reveal that they are more stable than 2D bilayer lead iodide perovskites. The trend in stability of the studied bilayer perovskites is C8BrN2 ≈ C7BrN2 > C6BrN2 > C4BrN2. Remarkably, in a reversal of the trend observed in the iodides, the $MAPbBr_3$ exhibits superior stability over the studied 2D lead bromide and 2D lead iodide perovskites under operating conditions. SS-PFM on the bilayer lead bromide thin films' surface presents a hysteretic behavior that is typical of ferroelectric polarization switching. This work underpins hybrid lead bromide perovskites as highly desirable materials for light-emission devices that would benefit from the impressive film stability and carrier lifetime.

■ ASSOCIATED CONTENT

Supporting Information

The Supporting Information is available free of charge at https://pubs.acs.org/doi/10.1021/acs.chemmater.1c01129.

X-ray crystallographic data for $(C6)_2(MA)Pb_2Br_7$ ($n = 2$) at 273 K (CIF)

X-ray crystallographic data for $(C6)_2(MA)Pb_2Br_7$ ($n = 2$) at 323 K (CIF)

X-ray crystallographic data for $(C7)_2(MA)Pb_2Br_7$ ($n = 2$) at 293 K (CIF)

X-ray crystallographic data for $(C8)_2(MA)Pb_2Br_7$ ($n = 2$) at 293 K (CIF)

X-ray crystallographic data for $(C8)_2(MA)Pb_2I_7$ ($n = 2$) at 293 K (CIF)

Methods, X-ray diffraction measurements, additional structural analysis, variable-temperature powder X-ray diffraction, thermal analysis, DFT calculations, stability tests, switching spectroscopy-piezoresponse force microscopy, and time-resolved photoluminescence under liquid nitrogen data (PDF)

■ AUTHOR INFORMATION

Corresponding Author

Mercouri G. Kanatzidis − *Department of Chemistry, Northwestern University, Evanston, Illinois 60208, United States;* orcid.org/0000-0003-2037-4168; Email: m-kanatzidis@northwestern.edu

Authors

Eugenia S. Vasileiadou − *Department of Chemistry, Northwestern University, Evanston, Illinois 60208, United States;* orcid.org/0000-0002-5714-9207

Ido Hadar − *Department of Chemistry, Northwestern University, Evanston, Illinois 60208, United States;* orcid.org/0000-0003-0576-9321

Mikaël Kepenekian − *Univ Rennes, ENSCR, CNRS, ISCR − UMR 6226, F-35000 Rennes, France;* orcid.org/0000-0001-5192-5896

Jacky Even − *Univ Rennes, INSA Rennes, CNRS, Institut FOTON − UMR 6082, F-35000 Rennes, France;* orcid.org/0000-0002-4607-3390

Qing Tu − *Department of Materials Science & Engineering, Northwestern University, Evanston, Illinois 60208, United States; Department of Materials Science & Engineering, Texas A&M University, College Station, Texas 77840, United States;* orcid.org/0000-0002-0445-6289

Christos D. Malliakas − *Department of Chemistry, Northwestern University, Evanston, Illinois 60208, United States;* orcid.org/0000-0003-4416-638X

Daniel Friedrich − *Department of Chemistry, Northwestern University, Evanston, Illinois 60208, United States*

Ioannis Spanopoulos − *Department of Chemistry, Northwestern University, Evanston, Illinois 60208, United States;* orcid.org/0000-0003-0861-1407

Justin M. Hoffman − *Department of Chemistry, Northwestern University, Evanston, Illinois 60208, United States;* orcid.org/0000-0003-1400-9180

Vinayak P. Dravid − *Department of Materials Science & Engineering, Northwestern University, Evanston, Illinois 60208, United States;* orcid.org/0000-0002-6007-3063

Complete contact information is available at: https://pubs.acs.org/10.1021/acs.chemmater.1c01129

Notes

The authors declare no competing financial interest.

■ ACKNOWLEDGMENTS

This work was supported by Department of Energy, Office of Science, Basic Energy Sciences, under grant SC0012541 (synthesis, structural, and optical characterization of materials). E.S.V. acknowledges the Dr. John N. Nicholson fellowship through Northwestern University. Q.T. acknowledges the startup funds from Texas A&M Engineering Experiment Station (TEES). This work made use of the NUANCE Center and IMSERC facilities of Northwestern University, which have received support from the Soft and Hybrid Nanotechnology Experimental (SHyNE) Resource (NSF ECCS-2025633), the MRSEC program (NSF DMR-1720139) at the Materials Research Center, the International Institute for Nanotechnology (IIN), the Keck Foundation, and the State of Illinois through the IIN. E.S.V. thanks Dr. Abishek Iyer, Dr. Tyler Slade, Michael A. Quintero, Craig Laing, and Benjamin Oxley for fruitful discussions.

■ REFERENCES

(1) Kojima, A.; Teshima, K.; Shirai, Y.; Miyasaka, T. Organometal Halide Perovskites as Visible-Light Sensitizers for Photovoltrafaic Cells. *J. Am. Chem. Soc.* **2009**, *131* (17), 6050−6051.

(2) Stoumpos, C. C.; Kanatzidis, M. G. The Renaissance of Halide Perovskites and Their Evolution as Emerging Semiconductors. *Acc. Chem. Res.* **2015**, *48* (10), 2791−2802.

(3) Stoumpos, C. C.; Kanatrafzidis, M. G. Halide Perovskites: Poor Man's High-Performance Semiconductors. *Adv. Mater.* **2016**, *28* (28), 5778−5793.

(4) Sutherland, B. R.; Sargent, E. H. Perovskite photonic sources. *Nat. Photonics* **2016**, *10*, 295.

(5) Lin, K.; Xing, J.; Quan, L. N.; de Arquer, F. P. G.; Gong, X.; Lu, J.; Xie, L.; Zhao, W.; Zhang, D.; Yan, C.; Li, W.; Liu, X.; Lu, Y.; Kirman, J.; Sargent, E. H.; Xiong, Q.; Wei, Z. Perovskite light-emitting diodes with external quantum efficiency exceeding 20%. *Nature* **2018**, *562* (7726), 245−248.

(6) Chung, I.; Lee, B.; He, J.; Chang, R. P. H.; Kanatzidis, M. G. All-solid-state dye-sensitized solar cells with high efficiency. *Nature* **2012**, *485* (7399), 486−489.

(7) Kim, H.-S.; Lee, C.-R.; Im, J.-H.; Lee, K.-B.; Moehl, T.; Marchioro, A.; Moon, S.-J.; Humphry-Baker, R.; Yum, J.-H.; Moser, J. E.; Grätzel, M.; Park, N.-G. Lead Iodide Perovskite Sensitized All-Solid-State Submicron Thin Film Mesoscopic Solar Cell with Efficiency Exceeding 9%. *Sci. Rep.* **2012**, *2* (1), 591.

(8) Lee, M. M.; Teuscher, J.; Miyasaka, T.; Murakami, T. N.; Snaith, H. J. Efficient Hybrid Solar Cells Based on Meso-Superstructured Organometal Halide Perovskites. *Science* **2012**, *338* (6107), 643.

(9) Stoumpos, C. C.; Malliakas, C. D.; Kanatzidis, M. G. Semiconducting Tin and Lead Iodide Perovskites with Organic Cations: Phase Transitions, High Mobilities, and Near-Infrared Photoluminescent Properties. *Inorg. Chem.* **2013**, *52* (15), 9019−9038.

(10) Stoumpos, C. C.; Cao, D. H.; Clark, D. J.; Young, J.; Rondinelli, J. M.; Jang, J. I.; Hupp, J. T.; Kanatzidis, M. G. Ruddlesden−Popper Hybrid Lead Iodide Perovskite 2D Homologous Semiconductors. *Chem. Mater.* **2016**, *28* (8), 2852−2867.

(11) Mączka, M.; Gagor, A.; Zaręba, J. K.; Stefanska, D.; Drozd, M.; Balciunas, S.; Šimėnas, M.; Banys, J.; Sieradzki, A. Three-Dimensional Perovskite Methylhydrazinium Lead Chloride with Two Polar Phases and Unusual Second-Harmonic Generation Bistability above Room Temperature. *Chem. Mater.* **2020**, *32* (9), 4072−4082.

(12) Mączka, M. a.; Ptak, M.; Gągor, A.; Stefańska, D.; Zaręba, J. K.; Sieradzki, A. Methylhydrazinium Lead Bromide: Noncentrosymmetric Three-Dimensional Perovskite with Exceptionally Large Framework Distortion and Green Photoluminescence. *Chem. Mater.* **2020**, *32* (4), 1667−1673.

(13) Goldschmidt, V. M. Die Gesetze der Krystallochemie. *Naturwissenschaften* **1926**, *14* (21), 477−485.

(14) Kieslich, G.; Sun, S.; Cheetham, A. K. Solid-state principles applied to organic−inorganic perovskites: new tricks for an old dog. *Chem. Sci.* **2014**, *5* (12), 4712−4715.

(15) Smith, I. C.; Hoke, E. T.; Solis-Ibarra, D.; McGehee, M. D.; Karunadasa, H. I. A Layered Hybrid Perovskite Solar-Cell Absorber with Enhanced Moisture Stability. *Angew. Chem., Int. Ed.* **2014**, *53* (42), 11232−11235.

(16) Cao, D. H.; Stoumpos, C. C.; Farha, O. K.; Hupp, J. T.; Kanatzidis, M. G. 2D Homologous Perovskites as Light-Absorbing Materials for Solar Cell Applications. *J. Am. Chem. Soc.* **2015**, *137* (24), 7843−7850.

(17) Niu, G.; Guo, X.; Wang, L. Review of recent progress in chemical stability of perovskite solar cells. *J. Mater. Chem. A* **2015**, *3* (17), 8970−8980.

(18) Quan, L. N.; Yuan, M.; Comin, R.; Voznyy, O.; Beauregard, E. M.; Hoogland, S.; Buin, A.; Kirmani, A. R.; Zhao, K.; Amassian, A.; Kim, D. H.; Sargent, E. H. Ligand-Stabilized Reduced-Dimensionality Perovskites. *J. Am. Chem. Soc.* **2016**, *138* (8), 2649−2655.

(19) Tsai, H.; Nie, W.; Blancon, J.-C.; Stoumpos, C. C.; Asadpour, R.; Harutyunyan, B.; Neukirch, A. J.; Verduzco, R.; Crochet, J. J.; Tretiak, S.; Pedesseau, L.; Even, J.; Alam, M. A.; Gupta, G.; Lou, J.; Ajayan, P. M.; Bedzyk, M. J.; Kanatzidis, M. G.; Mohite, A. D. High-efficiency two-dimensional Ruddlesden−Popper perovskite solar cells. *Nature* **2016**, *536*, 312.

(20) Zhao, X.; Ng, J. D. A.; Friend, R. H.; Tan, Z.-K. Opportunities and Challenges in Perovskite Light-Emitting Devices. *ACS Photonics* **2018**, *5* (10), 3866−3875.

(21) Mao, L.; Stoumpos, C. C.; Kanatzidis, M. G. Two-Dimensional Hybrid Halide Perovskites: Principles and Promises. *J. Am. Chem. Soc.* **2019**, *141* (3), 1171−1190.

(22) Smith, M. D.; Crace, E. J.; Jaffe, A.; Karunadasa, H. I. The Diversity of Layered Halide Perovskites. *Annu. Rev. Mater. Res.* **2018**, *48* (1), 111−136.

(23) Saparov, B.; Mitzi, D. B. Organic−Inorganic Perovskites: Structural Versatility for Functional Materials Design. *Chem. Rev.* **2016**, *116* (7), 4558−4596.

(24) Even, J.; Pedesseau, L.; Katan, C. Understanding Quantum Confinement of Charge Carriers in Layered 2D Hybrid Perovskites. *ChemPhysChem* **2014**, *15* (17), 3733−3741.

(25) Katan, C.; Mercier, N.; Even, J. Quantum and Dielectric Confinement Effects in Lower-Dimensional Hybrid Perovskite Semiconductors. *Chem. Rev.* **2019**, *119* (5), 3140−3192.

(26) Umeyama, D.; Lin, Y.; Karunadasa, H. I. Red-to-Black Piezochromism in a Compressible Pb−I−SCN Layered Perovskite. *Chem. Mater.* **2016**, *28* (10), 3241−3244.

(27) Li, X.; Hoffman, J.; Ke, W.; Chen, M.; Tsai, H.; Nie, W.; Mohite, A. D.; Kepenekian, M.; Katan, C.; Even, J.; Wasielewski, M. R.; Stoumpos, C. C.; Kanatzidis, M. G. Two-Dimensional Halide Perovskites Incorporating Straight Chain Symmetric Diammonium Ions, $(NH_3C_mH_{2m}NH_3)(CH_3NH_3)_{n-1}Pb_nI_{3n+1}$ (m = 4−9; n = 1−4). *J. Am. Chem. Soc.* **2018**, *140* (38), 12226−12238.

(28) Mao, L.; Ke, W.; Pedesseau, L.; Wu, Y.; Katan, C.; Even, J.; Wasielewski, M. R.; Stoumpos, C. C.; Kanatzidis, M. G. Hybrid Dion−Jacobson 2D Lead Iodide Perovskites. *J. Am. Chem. Soc.* **2018**, *140* (10), 3775−3783.

(29) Quintero-Bermudez, R.; Gold-Parker, A.; Proppe, A. H.; Munir, R.; Yang, Z.; Kelley, S. O.; Amassian, A.; Toney, M. F.; Sargent, E. H. Compositional and orientational control in metal halide perovskites of reduced dimensionality. *Nat. Mater.* **2018**, *17* (10), 900−907.

(30) Hadi, A.; Ryan, B. J.; Nelson, R. D.; Santra, K.; Lin, F.-Y.; Cochran, E. W.; Panthani, M. G. Improving the Stability and Monodispersity of Layered Cesium Lead Iodide Perovskite Thin Films by Tuning Crystallization Dynamics. *Chem. Mater.* **2019**, *31* (14), 4990−4998.

(31) Hoffman, J. M.; Che, X.; Sidhik, S.; Li, X.; Hadar, I.; Blancon, J.-C.; Yamaguchi, H.; Kepenekian, M.; Katan, C.; Even, J.; Stoumpos, C. C.; Mohite, A. D.; Kanatzidis, M. G. From 2D to 1D Electronic Dimensionality in Halide Perovskites with Stepped and Flat Layers Using Propylammonium as a Spacer. *J. Am. Chem. Soc.* **2019**, *141* (27), 10661−10676.

(32) Li, X.; Ke, W.; Traoré, B.; Guo, P.; Hadar, I.; Kepenekian, M.; Even, J.; Katan, C.; Stoumpos, C. C.; Schaller, R. D.; Kanatzidis, M. G. Two-Dimensional Dion−Jacobson Hybrid Lead Iodide Perovskites with Aromatic Diammonium Cations. *J. Am. Chem. Soc.* **2019**, *141* (32), 12880−12890.

(33) Li, T.; Zeidell, A. M.; Findik, G.; Dunlap-Shohl, W. A.; Euvrard, J.; Gundogdu, K.; Jurchescu, O. D.; Mitzi, D. B. Phase-Pure Hybrid Layered Lead Iodide Perovskite Films Based on a Two-Step Melt-Processing Approach. *Chem. Mater.* **2019**, *31* (11), 4267−4274.

(34) Spanopoulos, I.; Hadar, I.; Ke, W.; Tu, Q.; Chen, M.; Tsai, H.; He, Y.; Shekhawat, G.; Dravid, V. P.; Wasielewski, M. R.; Mohite, A. D.; Stoumpos, C. C.; Kanatzidis, M. G. Uniaxial Expansion of the 2D Ruddlesden−Popper Perovskite Family for Improved Environmental Stability. *J. Am. Chem. Soc.* **2019**, *141* (13), 5518−5534.

(35) Ramos-Terrón, S.; Jodlowski, A. D.; Verdugo-Escamilla, C.; Camacho, L.; de Miguel, G. Relaxing the Goldschmidt Tolerance Factor: Sizable Incorporation of the Guanidinium Cation into a Two-Dimensional Ruddlesden−Popper Perovskite. *Chem. Mater.* **2020**, *32* (9), 4024−4037.

(36) Billing, D. G.; Lemmerer, A. Synthesis, characterization and phase transitions in the inorganic-organic layered perovskite-type hybrids [(CnH2n + 1NH3)2PbI4], n = 4, 5 and 6. *Acta Crystallogr., Sect. B: Struct. Sci.* **2007**, *63* (5), 735−747.

(37) Lemmerer, A.; Billing, D. G. Lead halide inorganic−organic hybrids incorporating diammonium cations. *CrystEngComm* **2012**, *14* (6), 1954−1966.

(38) Lemmerer, A.; Billing, D. G. Synthesis, characterization and phase transitions of the inorganic−organic layered perovskite-type hybrids [(CnH2n+1NH3)2PbI4], n = 7, 8, 9 and 10. *Dalton Transactions* **2012**, *41* (4), 1146−1157.

(39) Milot, R. L.; Sutton, R. J.; Eperon, G. E.; Haghighirad, A. A.; Martinez Hardigree, J.; Miranda, L.; Snaith, H. J.; Johnston, M. B.; Herz, L. M. Charge-Carrier Dynamics in 2D Hybrid Metal−Halide Perovskites. *Nano Lett.* **2016**, *16* (11), 7001−7007.

(40) Yuan, M.; Quan, L. N.; Comin, R.; Walters, G.; Sabatini, R.; Voznyy, O.; Hoogland, S.; Zhao, Y.; Beauregard, E. M.; Kanjanaboos, P.; Lu, Z.; Kim, D. H.; Sargent, E. H. Perovskite energy funnels for efficient light-emitting diodes. *Nat. Nanotechnol.* **2016**, *11* (10), 872−877.

(41) Leng, K.; Abdelwahab, I.; Verzhbitskiy, I.; Telychko, M.; Chu, L.; Fu, W.; Chi, X.; Guo, N.; Chen, Z.; Chen, Z.; Zhang, C.; Xu, Q.-H.; Lu, J.; Chhowalla, M.; Eda, G.; Loh, K. P. Molecularly thin two-dimensional hybrid perovskites with tunable optoelectronic properties due to reversible surface relaxation. *Nat. Mater.* **2018**, *17* (10), 908−914.

(42) Oswald, I. W. H.; Koegel, A. A.; Neilson, J. R. General Synthesis Principles for Ruddlesden−Popper Hybrid Perovskite Halides from a Dynamic Equilibrium. *Chem. Mater.* **2018**, *30* (23), 8606−8614.

(43) Tsai, H.; Asadpour, R.; Blancon, J.-C.; Stoumpos, C. C.; Even, J.; Ajayan, P. M.; Kanatzidis, M. G.; Alam, M. A.; Mohite, A. D.; Nie, W. Design principles for electronic charge transport in solution-processed vertically stacked 2D perovskite quantum wells. *Nat. Commun.* **2018**, *9* (1), 2130.

(44) Zhang, Y.; Wang, P.; Tang, M.-C.; Barrit, D.; Ke, W.; Liu, J.; Luo, T.; Liu, Y.; Niu, T.; Smilgies, D.-M.; Yang, Z.; Liu, Z.; Jin, S.; Kanatzidis, M. G.; Amassian, A.; Liu, S. F.; Zhao, K. Dynamical Transformation of Two-Dimensional Perovskites with Alternating Cations in the Interlayer Space for High-Performance Photovoltaics. *J. Am. Chem. Soc.* **2019**, *141* (6), 2684−2694.

(45) Ke, W.; Mao, L.; Stoumpos, C. C.; Hoffman, J.; Spanopoulos, I.; Mohite, A. D.; Kanatzidis, M. G. Compositional and Solvent Engineering in Dion−Jacobson 2D Perovskites Boosts Solar Cell Efficiency and Stability. *Adv. Energy Mater.* **2019**, *9* (10), 1803384.

(46) Dahlman, C. J.; Venkatesan, N. R.; Corona, P. T.; Kennard, R. M.; Mao, L.; Smith, N. C.; Zhang, J.; Seshadri, R.; Helgeson, M. E.; Chabinyc, M. L. Structural Evolution of Layered Hybrid Lead Iodide Perovskites in Colloidal Dispersions. *ACS Nano* **2020**, *14* (9), 11294−11308.

(47) Hoffman, J. M.; Strzalka, J.; Flanders, N. C.; Hadar, I.; Cuthriell, S. A.; Zhang, Q.; Schaller, R. D.; Dichtel, W. R.; Chen, L. X.; Kanatzidis, M. G. In Situ Grazing-Incidence Wide-Angle Scattering Reveals Mechanisms for Phase Distribution and Disorientation in 2D Halide Perovskite Films. *Adv. Mater.* **2020**, *32* (33), e2002812.

(48) Ghosh, D.; Acharya, D.; Pedesseau, L.; Katan, C.; Even, J.; Tretiak, S.; Neukirch, A. J. Charge carrier dynamics in two-dimensional hybrid perovskites: Dion−Jacobson vs. Ruddlesden−Popper phases. *J. Mater. Chem. A* **2020**, *8* (42), 22009−22022.

(49) Hoffman, J. M.; Malliakas, C. D.; Sidhik, S.; Hadar, I.; McClain, R.; Mohite, A. D.; Kanatzidis, M. G. Long periodic ripple in a 2D hybrid halide perovskite structure using branched organic spacers. *Chem. Sci.* **2020**, *11* (44), 12139−12148.

(50) Li, X.; Fu, Y.; Pedesseau, L.; Guo, P.; Cuthriell, S.; Hadar, I.; Even, J.; Katan, C.; Stoumpos, C. C.; Schaller, R. D.; Harel, E.; Kanatzidis, M. G. Negative Pressure Engineering with Large Cage Cations in 2D Halide Perovskites Causes Lattice Softening. *J. Am. Chem. Soc.* **2020**, *142* (26), 11486−11496.

(51) Blancon, J.-C.; Even, J.; Stoumpos, C. C.; Kanatzidis, M. G.; Mohite, A. D. Semiconductor physics of organic−inorganic 2D halide perovskites. *Nat. Nanotechnol.* **2020**, *15* (12), 969−985.

(52) Petrov, A. A.; Fateev, S. A.; Khrustalev, V. N.; Li, Y.; Dorovatovskii, P. V.; Zubavichus, Y. V.; Goodilin, E. A.; Tarasov, A. B. Formamidinium Haloplumbate Intermediates: The Missing Link in a Chain of Hybrid Perovskites Crystallization. *Chem. Mater.* **2020**, *32* (18), 7739−7745.

(53) Xi, J.; Spanopoulos, I.; Bang, K.; Xu, J.; Dong, H.; Yang, Y.; Malliakas, C. D.; Hoffman, J. M.; Kanatzidis, M. G.; Wu, Z. Alternative Organic Spacers for More Efficient Perovskite Solar Cells Containing Ruddlesden-Popper Phases. *J. Am. Chem. Soc.* **2020**, *142* (46), 19705−19714.

(54) Li, X.; Hoffman, J. M.; Kanatzidis, M. G. The 2D Halide Perovskite Rulebook: How the Spacer Influences Everything from the Structure to Optoelectronic Device Efficiency. *Chem. Rev.* **2021**, *121* (4), 2230−2291.

(55) Spanopoulos, I.; Ke, W.; Kanatzidis, M. G. In Quest of Environmentally Stable Perovskite Solar Cells: A Perspective. *Helv. Chim. Acta* **2021**, *104* (1), e2000173.

(56) Vasileiadou, E. S.; Wang, B.; Spanopoulos, I.; Hadar, I.; Navrotsky, A.; Kanatzidis, M. G. Insight on the Stability of Thick Layers in 2D Ruddlesden−Popper and Dion−Jacobson Lead Iodide Perovskites. *J. Am. Chem. Soc.* **2021**, *143* (6), 2523−2536.

(57) Lanty, G.; Jemli, K.; Wei, Y.; Leymarie, J.; Even, J.; Lauret, J.-S.; Deleporte, E. Room-Temperature Optical Tunability and Inhomogeneous Broadening in 2D-Layered Organic−Inorganic Perovskite Pseudobinary Alloys. *J. Phys. Chem. Lett.* **2014**, *5* (22), 3958−3963.

(58) Corradi, A. B.; Ferrari, A. M.; Pellacani, G. C.; Saccani, A.; Sandrolini, F.; Sgarabotto, P. Structural and Electrical Characterization of Polymeric Haloplumbate(II) Systems. *Inorg. Chem.* **1999**, *38* (4), 716−721.

(59) Mitzi, D. B. A Layered Solution Crystal Growth Technique and the Crystal Structure of (C6H5C2H4NH3)2PbCl4. *J. Solid State Chem.* **1999**, *145* (2), 694−704.

(60) Mitzi, D. B.; Chondroudis, K.; Kagan, C. R. Design, Structure, and Optical Properties of Organic−Inorganic Perovskites Containing an Oligothiophene Chromophore. *Inorg. Chem.* **1999**, *38* (26), 6246−6256.

(61) Bonamartini Corradi, A.; Ferrari, A. M.; Righi, L.; Sgarabotto, P. An Additional Structural and Electrical Study of Polymeric Haloplumbates(II) with Heterocyclic Diprotonated Amines. *Inorg. Chem.* **2001**, *40* (2), 218−223.

(62) Tanaka, K.; Takahashi, T.; Kondo, T.; Umeda, K.; Ema, K.; Umebayashi, T.; Asai, K.; Uchida, K.; Miura, N. Electronic and Excitonic Structures of Inorganic−Organic Perovskite-Type Quantum-Well Crystal (C4H9NH3)2PbBr4. *Jpn. J. Appl. Phys.* **2005**, *44* (8), 5923−5932.

(63) Billing, D. G.; Lemmerer, A. Inorganic−organic hybrid materials incorporating primary cyclic ammonium cations: The lead bromide and chloride series. *CrystEngComm* **2009**, *11* (8), 1549−1562.

(64) Rayner, M. K.; Billing, D. G. Poly[1,4-bis(ammoniomethyl)-cyclohexane [di-[mu]-bromido-dibromidoplumbate(II)]]. *Acta Crystallogr., Sect. E: Struct. Rep. Online* **2010**, *66* (6), m658.

(65) Kitazawa, N.; Aono, M.; Watanabe, Y. Excitons in organic−inorganic hybrid compounds (CnH2n+1NH3)2PbBr4 (n = 4, 5, 7 and 12). *Thin Solid Films* **2010**, *518* (12), 3199−3203.

(66) Yamamoto, Y.; Oohata, G.; Mizoguchi, K.; Ichida, H.; Kanematsu, Y. Photoluminescence of excitons and biexcitons in (C4H9NH3)2PbBr4 crystals under high excitation density. *physica status solidi c* **2012**, *9* (12), 2501−2504.

(67) Dou, L.; Wong, A. B.; Yu, Y.; Lai, M.; Kornienko, N.; Eaton, S. W.; Fu, A.; Bischak, C. G.; Ma, J.; Ding, T.; Ginsberg, N. S.; Wang, L.-W.; Alivisatos, A. P.; Yang, P. Atomically thin two-dimensional organic-inorganic hybrid perovskites. *Science* **2015**, *349* (6255), 1518.

(68) Liao, W.-Q.; Zhang, Y.; Hu, C.-L.; Mao, J.-G.; Ye, H.-Y.; Li, P.-F.; Huang, S. D.; Xiong, R.-G. A Lead-Halide Perovskite Molecular Ferroelectric Semiconductor. *Nat. Commun.* **2015**, *6* (1), 7338.

(69) Ye, H.-Y.; Liao, W.-Q.; Hu, C.-L.; Zhang, Y.; You, Y.-M.; Mao, J.-G.; Li, P.-F.; Xiong, R.-G. Bandgap Engineering of Lead-Halide Perovskite-Type Ferroelectrics. *Adv. Mater.* **2016**, *28* (13), 2579−2586.

(70) Du, K.-z.; Tu, Q.; Zhang, X.; Han, Q.; Liu, J.; Zauscher, S.; Mitzi, D. B. Two-Dimensional Lead(II) Halide-Based Hybrid Perovskites Templated by Acene Alkylamines: Crystal Structures, Optical Properties, and Piezoelectricity. *Inorg. Chem.* **2017**, *56* (15), 9291−9302.

(71) Smith, M. D.; Jaffe, A.; Dohner, E. R.; Lindenberg, A. M.; Karunadasa, H. I. Structural origins of broadband emission from layered Pb−Br hybrid perovskites. *Chem. Sci.* **2017**, *8* (6), 4497−4504.

(72) Ortiz-Cervantes, C.; Román-Román, P. I.; Vazquez-Chavez, J.; Hernández-Rodríguez, M.; Solis-Ibarra, D. Thousand-fold Conduc-

tivity Increase in 2D Perovskites by Polydiacetylene Incorporation and Doping. *Angew. Chem., Int. Ed.* **2018**, *57* (42), 13882−13886.

(73) Xiao, J.; Chang, J.; Li, B.; Isikgor, F. H.; Wang, D.; Fan, Z.; Lin, Z.; Ouyang, J.; Zeng, K.; Chen, J. Room temperature ferroelectricity of hybrid organic−inorganic perovskites with mixed iodine and bromine. *J. Mater. Chem. A* **2018**, *6* (20), 9665−9676.

(74) Chen, X.-G.; Song, X.-J.; Zhang, Z.-X.; Li, P.-F.; Ge, J.-Z.; Tang, Y.-Y.; Gao, J.-X.; Zhang, W.-Y.; Fu, D.-W.; You, Y.-M.; Xiong, R.-G. Two-Dimensional Layered Perovskite Ferroelectric with Giant Piezoelectric Voltage Coefficient. *J. Am. Chem. Soc.* **2020**, *142* (2), 1077−1082.

(75) Guo, Y.-Y.; Yang, L.-J.; Biberger, S.; McNulty, J. A.; Li, T.; Schötz, K.; Panzer, F.; Lightfoot, P. Structural Diversity in Layered Hybrid Perovskites, A2PbBr4 or AA′PbBr4, Templated by Small Disc-Shaped Amines. *Inorg. Chem.* **2020**, *59* (17), 12858−12866.

(76) Huang, G.; Rassel, S.; Qu, J.; Xu, S.; Wang, C.; Ban, D. Manipulation of Spin Splitting in Two-Dimensional Lead Bromide Perovskite Rashba Piezoelectrics. *ACS Applied Electronic Materials* **2021**, *3* (1), 285−291.

(77) Li, Y. Y.; Lin, C. K.; Zheng, G. L.; Cheng, Z. Y.; You, H.; Wang, W. D.; Lin, J. Novel ⟨110⟩-Oriented Organic−Inorganic Perovskite Compound Stabilized by N-(3-Aminopropyl)imidazole with Improved Optical Properties. *Chem. Mater.* **2006**, *18* (15), 3463−3469.

(78) Dohner, E. R.; Hoke, E. T.; Karunadasa, H. I. Self-Assembly of Broadband White-Light Emitters. *J. Am. Chem. Soc.* **2014**, *136* (5), 1718−1721.

(79) Dohner, E. R.; Jaffe, A.; Bradshaw, L. R.; Karunadasa, H. I. Intrinsic White-Light Emission from Layered Hybrid Perovskites. *J. Am. Chem. Soc.* **2014**, *136* (38), 13154−13157.

(80) Mao, L.; Wu, Y.; Stoumpos, C. C.; Wasielewski, M. R.; Kanatzidis, M. G. White-Light Emission and Structural Distortion in New Corrugated Two-Dimensional Lead Bromide Perovskites. *J. Am. Chem. Soc.* **2017**, *139* (14), 5210−5215.

(81) Mao, L.; Wu, Y.; Stoumpos, C. C.; Traore, B.; Katan, C.; Even, J.; Wasielewski, M. R.; Kanatzidis, M. G. Tunable White-Light Emission in Single-Cation-Templated Three-Layered 2D Perovskites (CH3CH2NH3)4Pb3Br10−xClx. *J. Am. Chem. Soc.* **2017**, *139* (34), 11956−11963.

(82) Mao, L.; Guo, P.; Kepenekian, M.; Hadar, I.; Katan, C.; Even, J.; Schaller, R. D.; Stoumpos, C. C.; Kanatzidis, M. G. Structural Diversity in White-Light-Emitting Hybrid Lead Bromide Perovskites. *J. Am. Chem. Soc.* **2018**, *140* (40), 13078−13088.

(83) Guo, Y.-Y.; McNulty, J. A.; Mica, N. A.; Samuel, I. D. W.; Slawin, A. M. Z.; Bühl, M.; Lightfoot, P. Structure-directing effects in (110)-layered hybrid perovskites containing two distinct organic moieties. *Chem. Commun.* **2019**, *55* (67), 9935−9938.

(84) Li, X.; Guo, P.; Kepenekian, M.; Hadar, I.; Katan, C.; Even, J.; Stoumpos, C. C.; Schaller, R. D.; Kanatzidis, M. G. Small Cyclic Diammonium Cation Templated (110)-Oriented 2D Halide (X = I, Br, Cl) Perovskites with White-Light Emission. *Chem. Mater.* **2019**, *31* (9), 3582−3590.

(85) Salah, M. B. H.; Mercier, N.; Allain, M.; Zouari, N.; Giovanella, U.; Botta, C. Mechanochromic and Electroluminescence Properties of a Layered Hybrid Perovskite Belonging to the < 110> Series. *Eur. J. Inorg. Chem.* **2019**, *2019* (42), 4527−4531.

(86) Febriansyah, B.; Giovanni, D.; Ramesh, S.; Koh, T. M.; Li, Y.; Sum, T. C.; Mathews, N.; England, J. Inducing formation of a corrugated, white-light emitting 2D lead-bromide perovskite via subtle changes in templating cation. *J. Mater. Chem. C* **2020**, *8* (3), 889−893.

(87) Gomez, V.; Klyatskaya, S.; Fuhr, O.; Kalytchuk, S.; Zboril, R.; Kappes, M.; Lebedkin, S.; Ruben, M. Pressure-Modulated Broadband Emission in 2D Layered Hybrid Perovskite-Like Bromoplumbate. *Inorg. Chem.* **2020**, *59* (17), 12431−12436.

(88) Yan, S. Y.; Tian, W. L.; Chen, H.; Tang, K. X.; Lin, T. T.; Zhong, G. Y.; Qiu, L. Z.; Pan, X. Y.; Wang, W. Z. Deep Blue Layered Lead Perovskite Light-Emitting Diode. *Adv. Opt. Mater.* **2021**, *9* (4), 2001709.

(89) Krummer, M.; Zimmermann, B.; Klingenberg, P.; Daub, M.; Hillebrecht, H. Perovskite-Related 2D Compounds in the System 5-Amino Valerian Acid Cation/MA/Pb/X (X = Cl, Br) − Synthesis, Crystal Structures, and Optical Properties. *Eur. J. Inorg. Chem.* **2020**, *2020* (48), 4581−4592.

(90) Calabrese, J.; Jones, N. L.; Harlow, R. L.; Herron, N.; Thorn, D. L.; Wang, Y. Preparation and characterization of layered lead halide compounds. *J. Am. Chem. Soc.* **1991**, *113* (6), 2328−2330.

(91) Li, L.; Sun, Z.; Wang, P.; Hu, W.; Wang, S.; Ji, C.; Hong, M.; Luo, J. Tailored Engineering of an Unusual (C4H9NH3)2-(CH3NH3)2Pb3Br10 Two-Dimensional Multilayered Perovskite Ferroelectric for a High-Performance Photodetector. *Angew. Chem., Int. Ed.* **2017**, *56* (40), 12150−12154.

(92) Tabuchi, Y.; Asai, K.; Rikukawa, M.; Sanui, K.; Ishigure, K. Preparation and characterization of natural lower dimensional layered perovskite-type compounds. *J. Phys. Chem. Solids* **2000**, *61* (6), 837−845.

(93) Nazarenko, O.; Kotyrba, M. R.; Wörle, M.; Cuervo-Reyes, E.; Yakunin, S.; Kovalenko, M. V. Luminescent and Photoconductive Layered Lead Halide Perovskite Compounds Comprising Mixtures of Cesium and Guanidinium Cations. *Inorg. Chem.* **2017**, *56* (19), 11552−11564.

(94) Li, L.; Shang, X.; Wang, S.; Dong, N.; Ji, C.; Chen, X.; Zhao, S.; Wang, J.; Sun, Z.; Hong, M.; Luo, J. Bilayered Hybrid Perovskite Ferroelectric with Giant Two-Photon Absorption. *J. Am. Chem. Soc.* **2018**, *140* (22), 6806−6809.

(95) Wu, Z.; Ji, C.; Li, L.; Kong, J.; Sun, Z.; Zhao, S.; Wang, S.; Hong, M.; Luo, J. Alloying n-Butylamine into CsPbBr3 To Give a Two-Dimensional Bilayered Perovskite Ferroelectric Material. *Angew. Chem., Int. Ed.* **2018**, *57* (27), 8140−8143.

(96) Li, L.; Liu, X.; Li, Y.; Xu, Z.; Wu, Z.; Han, S.; Tao, K.; Hong, M.; Luo, J.; Sun, Z. Two-Dimensional Hybrid Perovskite-Type Ferroelectric for Highly Polarization-Sensitive Shortwave Photodetection. *J. Am. Chem. Soc.* **2019**, *141* (6), 2623−2629.

(97) Wang, S.; Liu, X.; Li, L.; Ji, C.; Sun, Z.; Wu, Z.; Hong, M.; Luo, J. An Unprecedented Biaxial Trilayered Hybrid Perovskite Ferroelectric with Directionally Tunable Photovoltaic Effects. *J. Am. Chem. Soc.* **2019**, *141* (19), 7693−7697.

(98) Wu, Z.; Liu, X.; Ji, C.; Li, L.; Wang, S.; Peng, Y.; Tao, K.; Sun, Z.; Hong, M.; Luo, J. Discovery of an Above-Room-Temperature Antiferroelectric in Two-Dimensional Hybrid Perovskite. *J. Am. Chem. Soc.* **2019**, *141* (9), 3812−3816.

(99) Chen, H.; Lin, J.; Kang, J.; Kong, Q.; Lu, D.; Kang, J.; Lai, M.; Quan, L. N.; Lin, Z.; Jin, J.; Wang, L. W.; Toney, M. F.; Yang, P. Structural and spectral dynamics of single-crystalline Ruddlesden-Popper phase halide perovskite blue light-emitting diodes. *Sci. Adv.* **2020**, *6* (4), eaay4045.

(100) Li, H.; Qin, Y.; Shan, B.; Shen, Y.; Ersan, F.; Soignard, E.; Ataca, C.; Tongay, S. Unusual Pressure-Driven Phase Transformation and Band Renormalization in 2D vdW Hybrid Lead Halide Perovskites. *Adv. Mater.* **2020**, *32* (12), e1907364.

(101) Paritmongkol, W.; Dahod, N. S.; Stollmann, A.; Mao, N.; Settens, C.; Zheng, S.-L.; Tisdale, W. A. Synthetic Variation and Structural Trends in Layered Two-Dimensional Alkylammonium Lead Halide Perovskites. *Chem. Mater.* **2019**, *31* (15), 5592−5607.

(102) Peng, Y.; Bie, J.; Liu, X.; Li, L.; Chen, S.; Fa, W.; Wang, S.; Sun, Z.; Luo, J. Acquiring High-TC Layered Metal Halide Ferroelectrics via Cage-Confined Ethylamine Rotators. *Angew. Chem., Int. Ed.* **2021**, *60* (6), 2839−2843.

(103) Mao, L.; Guo, P.; Kepenekian, M.; Spanopoulos, I.; He, Y.; Katan, C.; Even, J.; Schaller, R. D.; Seshadri, R.; Stoumpos, C. C.; Kanatzidis, M. G. Organic Cation Alloying on Intralayer A and Interlayer A' sites in 2D Hybrid Dion-Jacobson Lead Bromide Perovskites (A')(A)Pb2Br7. *J. Am. Chem. Soc.* **2020**, *142*, 8342.

(104) Ji, C.; Dey, D.; Peng, Y.; Liu, X.; Li, L.; Luo, J. Ferroelectricity-Driven Self-Powered Ultraviolet Photodetection with Strong Polarization Sensitivity in a Two-Dimensional Halide Hybrid Perovskite. *Angew. Chem., Int. Ed.* **2020**, *59* (43), 18933−18937.

(105) Nandi, P.; Topwal, D.; Park, N.-G.; Shin, H. Organic-inorganic hybrid lead halides as absorbers in perovskite solar cells: a

debate on ferroelectricity. *J. Phys. D: Appl. Phys.* **2020**, *53* (49), 493002.

(106) Yao, Y.; Peng, Y.; Li, L.; Zhang, X.; Liu, X.; Hong, M.; Luo, J. Exploring a Fatigue-Free Layered Hybrid Perovskite Ferroelectric for Photovoltaic Non-Volatile Memories. *Angew. Chem., Int. Ed.* **2021**, *60*, 10598.

(107) Zhang, H. Y.; Zhang, Z. X.; Song, X. J.; Chen, X. G.; Xiong, R. G. Two-Dimensional Hybrid Perovskite Ferroelectric Induced by Perfluorinated Substitution. *J. Am. Chem. Soc.* **2020**, *142* (47), 20208−20215.

(108) Zhang, H. Y.; Zhang, Z. X.; Chen, X. G.; Song, X. J.; Zhang, Y.; Xiong, R. G. Large Electrostrictive Coefficient in a Two-Dimensional Hybrid Perovskite Ferroelectric. *J. Am. Chem. Soc.* **2021**, *143* (3), 1664−1672.

(109) Liu, Y.; Han, S.; Wang, J.; Ma, Y.; Guo, W.; Huang, X.-Y.; Luo, J.-H.; Hong, M.; Sun, Z. Spacer Cation Alloying of a Homoconformational Carboxylate trans Isomer to Boost in-Plane Ferroelectricity in a 2D Hybrid Perovskite. *J. Am. Chem. Soc.* **2021**, *143* (4), 2130−2137.

(110) Peng, Y.; Bie, J.; Liu, X.; Li, L.; Chen, S.; Fa, W.; Wang, S.; Sun, Z.; Luo, J. Acquiring High-TC Layered Metal Halide Ferroelectrics via Cage-Confined Ethylamine Rotators. *Angew. Chem., Int. Ed.* **2021**, *60* (6), 2839−2843.

(111) Wang, Z.; Wang, F.; Sun, W.; Ni, R.; Hu, S.; Liu, J.; Zhang, B.; Alsaed, A.; Hayat, T.; Tan, Z. a. Manipulating the Trade-off Between Quantum Yield and Electrical Conductivity for High-Brightness Quasi-2D Perovskite Light-Emitting Diodes. *Adv. Funct. Mater.* **2018**, *28* (47), 1804187.

(112) Yang, X.; Zhang, X.; Deng, J.; Chu, Z.; Jiang, Q.; Meng, J.; Wang, P.; Zhang, L.; Yin, Z.; You, J. Efficient green light-emitting diodes based on quasi-two-dimensional composition and phase engineered perovskite with surface passivation. *Nat. Commun.* **2018**, *9* (1), 570.

(113) Zhao, B.; Bai, S.; Kim, V.; Lamboll, R.; Shivanna, R.; Auras, F.; Richter, J. M.; Yang, L.; Dai, L.; Alsari, M.; She, X.-J.; Liang, L.; Zhang, J.; Lilliu, S.; Gao, P.; Snaith, H. J.; Wang, J.; Greenham, N. C.; Friend, R. H.; Di, D. High-efficiency perovskite−polymer bulk heterostructure light-emitting diodes. *Nat. Photonics* **2018**, *12* (12), 783−789.

(114) Han, Y.; Park, S.; Kim, C.; Lee, M.; Hwang, I. Phase control of quasi-2D perovskites and improved light-emitting performance by excess organic cations and nanoparticle intercalation. *Nanoscale* **2019**, *11* (8), 3546−3556.

(115) Li, C. H. A.; Zhou, Z.; Vashishtha, P.; Halpert, J. E. The Future Is Blue (LEDs): Why Chemistry Is the Key to Perovskite Displays. *Chem. Mater.* **2019**, *31* (16), 6003−6032.

(116) Ng, Y. F.; Febriansyah, B.; Jamaludin, N. F.; Giovanni, D.; Yantara, N.; Chin, X. Y.; Tay, Y. B.; Sum, T. C.; Mhaisalkar, S.; Mathews, N. Design of 2D Templating Molecules for Mixed-Dimensional Perovskite Light-Emitting Diodes. *Chem. Mater.* **2020**, *32* (19), 8097−8105.

(117) Tsai, H.; Liu, C.; Kinigstein, E.; Li, M.; Tretiak, S.; Cotlet, M.; Ma, X.; Zhang, X.; Nie, W. Critical Role of Organic Spacers for Bright 2D Layered Perovskites Light-Emitting Diodes. *Advanced Science* **2020**, *7* (7), 1903202.

(118) Zhou, G.; Xu, Y.; Xia, Z. Perovskite Multiple Quantum Wells on Layered Materials toward Narrow-Band Green Emission for Backlight Display Applications. *ACS Appl. Mater. Interfaces* **2020**, *12* (24), 27386−27393.

(119) Liu, Y. L.; Yu, Z. K.; Chen, S.; Park, J. H.; Jung, E. D.; Lee, S.; Kang, K.; Ko, S. J.; Lim, J.; Song, M. H.; Xu, B. M.; Snaith, H. J.; Park, S. H.; Lee, B. R. Boosting the efficiency of quasi-2D perovskites light-emitting diodes by using encapsulation growth method. *Nano Energy* **2021**, *80*, 105511.

(120) Watanabe, S.; Tumen-Ulzii, G.; Cheng, T.; Matsushima, T.; Adachi, C. Origin and Suppression of External Quantum Efficiency Roll-Off in Quasi-Two-Dimensional Metal Halide Perovskite Light-Emitting Diodes. *J. Phys. Chem. C* **2020**, *124* (50), 27422−27428.

(121) Sun, X.; Han, C.; Liu, Z.; Xu, L.; Li, J.; Yu, H.; Wang, K. Effectiveness of Solvent Vapor Annealing on Optoelectronic Properties for Quasi-2D Organic−Inorganic Hybrid Perovskite Light-Emitting Diodes. *J. Phys. Chem. C* **2020**, *124* (52), 28417−28423.

(122) Gong, X.; Voznyy, O.; Jain, A.; Liu, W.; Sabatini, R.; Piontkowski, Z.; Walters, G.; Bappi, G.; Nokhrin, S.; Bushuyev, O.; Yuan, M.; Comin, R.; McCamant, D.; Kelley, S. O.; Sargent, E. H. Electron−phonon interaction in efficient perovskite blue emitters. *Nat. Mater.* **2018**, *17* (6), 550−556.

(123) Mao, L.; Kennard, R. M.; Traore, B.; Ke, W.; Katan, C.; Even, J.; Chabinyc, M. L.; Stoumpos, C. C.; Kanatzidis, M. G. Seven-Layered 2D Hybrid Lead Iodide Perovskites. *Chem.* **2019**, *5* (10), 2593−2604.

(124) Stoumpos, C. C.; Soe, C. M. M.; Tsai, H.; Nie, W.; Blancon, J.-C.; Cao, D. H.; Liu, F.; Traoré, B.; Katan, C.; Even, J.; Mohite, A. D.; Kanatzidis, M. G. High Members of the 2D Ruddlesden-Popper Halide Perovskites: Synthesis, Optical Properties, and Solar Cells of (CH3(CH2)3NH3)2(CH3NH3)4Pb5I16. *Chem.* **2017**, *2* (3), 427−440.

(125) Kepenekian, M.; Traore, B.; Blancon, J.-C.; Pedesseau, L.; Tsai, H.; Nie, W.; Stoumpos, C. C.; Kanatzidis, M. G.; Even, J.; Mohite, A. D.; Tretiak, S.; Katan, C. Concept of Lattice Mismatch and Emergence of Surface States in Two-dimensional Hybrid Perovskite Quantum Wells. *Nano Lett.* **2018**, *18* (9), 5603−5609.

(126) Tu, Q.; Spanopoulos, I.; Hao, S.; Wolverton, C.; Kanatzidis, M. G.; Shekhawat, G. S.; Dravid, V. P. Out-of-Plane Mechanical Properties of 2D Hybrid Organic−Inorganic Perovskites by Nanoindentation. *ACS Appl. Mater. Interfaces* **2018**, *10* (26), 22167−22173.

(127) Tu, Q.; Spanopoulos, I.; Yasaei, P.; Stoumpos, C. C.; Kanatzidis, M. G.; Shekhawat, G. S.; Dravid, V. P. Stretching and Breaking of Ultrathin 2D Hybrid Organic−Inorganic Perovskites. *ACS Nano* **2018**, *12* (10), 10347−10354.

(128) Tu, Q.; Spanopoulos, I.; Hao, S.; Wolverton, C.; Kanatzidis, M. G.; Shekhawat, G. S.; Dravid, V. P. Probing Strain-Induced Band Gap Modulation in 2D Hybrid Organic−Inorganic Perovskites. *ACS Energy Lett.* **2019**, *4* (3), 796−802.

(129) Tu, Q.; Spanopoulos, I.; Vasileiadou, E. S.; Li, X.; Kanatzidis, M. G.; Shekhawat, G. S.; Dravid, V. P. Exploring the Factors Affecting the Mechanical Properties of 2D Hybrid Organic-Inorganic Perovskites. *ACS Appl. Mater. Interfaces* **2020**, *12* (18), 20440−20447.

(130) Hamilton, W. Significance tests on the crystallographic R factor. *Acta Crystallogr.* **1965**, *18* (3), 502−510.

(131) Panuganti, S.; Besteiro, L. V.; Vasileiadou, E. S.; Hoffman, J. M.; Govorov, A. O.; Gray, S. K.; Kanatzidis, M. G.; Schaller, R. D. Distance Dependence of Forster Resonance Energy Transfer Rates in 2D Perovskite Quantum Wells via Control of Organic Spacer Length. *J. Am. Chem. Soc.* **2021**, *143* (11), 4244−4252.

(132) McClure, E. T.; McCormick, A. P.; Woodward, P. M. Four Lead-free Layered Double Perovskites with the n = 1 Ruddlesden−Popper Structure. *Inorg. Chem.* **2020**, *59* (9), 6010−6017.

(133) Knutson, J. L.; Martin, J. D.; Mitzi, D. B. Tuning the Band Gap in Hybrid Tin Iodide Perovskite Semiconductors Using Structural Templating. *Inorg. Chem.* **2005**, *44* (13), 4699−4705.

(134) Katan, C.; Pedesseau, L.; Kepenekian, M.; Rolland, A.; Even, J. Interplay of spin−orbit coupling and lattice distortion in metal substituted 3D tri-chloride hybrid perovskites. *J. Mater. Chem. A* **2015**, *3* (17), 9232−9240.

(135) Traore, B.; Pedesseau, L.; Assam, L.; Che, X.; Blancon, J.-C.; Tsai, H.; Nie, W.; Stoumpos, C. C.; Kanatzidis, M. G.; Tretiak, S.; Mohite, A. D.; Even, J.; Kepenekian, M.; Katan, C. Composite Nature of Layered Hybrid Perovskites: Assessment on Quantum and Dielectric Confinements and Band Alignment. *ACS Nano* **2018**, *12* (4), 3321−3332.

(136) Gate, L. F. Comparison of the Photon Diffusion Model and Kubelka-Munk Equation with the Exact Solution of the Radiative Transport Equation. *Appl. Opt.* **1974**, *13* (2), 236−238.

(137) Gonzalez-Carrero, S.; Espallargas, G. M.; Galian, R. E.; Pérez-Prieto, J. Blue-luminescent organic lead bromide perovskites: highly dispersible and photostable materials. *J. Mater. Chem. A* **2015**, *3* (26), 14039−14045.

(138) Zhou, G.; Xu, Y.; Xia, Z. Perovskite Multiple Quantum Wells on Layered Materials toward Narrow-Band Green Emission for Backlight Display Applications. *ACS Appl. Mater. Interfaces* **2020**, *12* (24), 27386−27393.

(139) Quan, L. N.; Zhao, Y.; García de Arquer, F. P.; Sabatini, R.; Walters, G.; Voznyy, O.; Comin, R.; Li, Y.; Fan, J. Z.; Tan, H.; Pan, J.; Yuan, M.; Bakr, O. M.; Lu, Z.; Kim, D. H.; Sargent, E. H. Tailoring the Energy Landscape in Quasi-2D Halide Perovskites Enables Efficient Green-Light Emission. *Nano Lett.* **2017**, *17* (6), 3701−3709.

(140) Wang, K.-H.; Li, L.-C.; Shellaiah, M.; Wen Sun, K. Structural and Photophysical Properties of Methylammonium Lead Tribromide (MAPbBr3) Single Crystals. *Sci. Rep.* **2017**, *7* (1), 13643.

(141) Kawano, N.; Koshimizu, M.; Sun, Y.; Yahaba, N.; Fujimoto, Y.; Yanagida, T.; Asai, K. Effects of Organic Moieties on Luminescence Properties of Organic−Inorganic Layered Perovskite-Type Compounds. *J. Phys. Chem. C* **2014**, *118* (17), 9101−9106.

(142) Chakraborty, R.; Nag, A. Correlation of Dielectric Confinement and Excitonic Binding Energy in 2D Layered Hybrid Perovskites Using Temperature Dependent Photoluminescence. *J. Phys. Chem. C* **2020**, *124* (29), 16177−16185.

(143) King-Smith, R. D.; Vanderbilt, D. Theory of polarization of crystalline solids. *Phys. Rev. B: Condens. Matter Mater. Phys.* **1993**, *47* (3), 1651−1654.

(144) Neaton, J. B.; Ederer, C.; Waghmare, U. V.; Spaldin, N. A.; Rabe, K. M. First-principles study of spontaneous polarization in multiferroic $\mathrm{Bi}\mathrm{Fe}{\mathrm{O}}_{3}$. *Phys. Rev. B: Condens. Matter Mater. Phys.* **2005**, *71* (1), 014113.

(145) Kepenekian, M.; Even, J. Rashba and Dresselhaus Couplings in Halide Perovskites: Accomplishments and Opportunities for Spintronics and Spin−Orbitronics. *J. Phys. Chem. Lett.* **2017**, *8* (14), 3362−3370.

(146) Dyksik, M.; Duim, H.; Zhu, X.; Yang, Z.; Gen, M.; Kohama, Y.; Adjokatse, S.; Maude, D. K.; Loi, M. A.; Egger, D. A.; Baranowski, M.; Plochocka, P. Broad Tunability of Carrier Effective Masses in Two-Dimensional Halide Perovskites. *ACS Energy Lett.* **2020**, *5*, 3609−3616.

(147) Fang, H.-H.; Raissa, R.; Abdu-Aguye, M.; Adjokatse, S.; Blake, G. R.; Even, J.; Loi, M. A. Photophysics of Organic−Inorganic Hybrid Lead Iodide Perovskite Single Crystals. *Adv. Funct. Mater.* **2015**, *25* (16), 2378−2385.

(148) Ghosh, D.; Neukirch, A. J.; Tretiak, S. Optoelectronic Properties of Two-Dimensional Bromide Perovskites: Influences of Spacer Cations. *J. Phys. Chem. Lett.* **2020**, *11*, 2955−2964.

(149) Ferreira, A. C.; Létoublon, A.; Paofai, S.; Raymond, S.; Ecolivet, C.; Rufflé, B.; Cordier, S.; Katan, C.; Saidaminov, M. I.; Zhumekenov, A. A.; Bakr, O. M.; Even, J.; Bourges, P. Elastic Softness of Hybrid Lead Halide Perovskites. *Phys. Rev. Lett.* **2018**, *121* (8), 085502.

(150) Hu, Y.; Spies, L. M.; Alonso-Álvarez, D.; Mocherla, P.; Jones, H.; Hanisch, J.; Bein, T.; Barnes, P. R. F.; Docampo, P. Identifying and controlling phase purity in 2D hybrid perovskite thin films. *J. Mater. Chem. A* **2018**, *6* (44), 22215−22225.

(151) Leung, T. L.; Tam, H. W.; Liu, F.; Lin, J.; Ng, A. M. C.; Chan, W. K.; Chen, W.; He, Z.; Lončarić, I.; Grisanti, L.; Ma, C.; Wong, K. S.; Lau, Y. S.; Zhu, F.; Skoko, Ž.; Popović, J.; Djurišić, A. B. Mixed Spacer Cation Stabilization of Blue-Emitting n = 2 Ruddlesden−Popper Organic−Inorganic Halide Perovskite Films. *Adv. Opt. Mater.* **2020**, *8* (4), 1901679.

(152) Wang, N.; Cheng, L.; Ge, R.; Zhang, S.; Miao, Y.; Zou, W.; Yi, C.; Sun, Y.; Cao, Y.; Yang, R.; Wei, Y.; Guo, Q.; Ke, Y.; Yu, M.; Jin, Y.; Liu, Y.; Ding, Q.; Di, D.; Yang, L.; Xing, G.; Tian, H.; Jin, C.; Gao, F.; Friend, R. H.; Wang, J.; Huang, W. Perovskite light-emitting diodes based on solution-processed self-organized multiple quantum wells. *Nat. Photonics* **2016**, *10* (11), 699−704.

(153) Wang, R.; Tong, Y.; Wang, K.; Xia, S.; Kentzinger, E.; Soltwedel, O.; Müller-Buschbaum, P.; Frielinghaus, H. Monitoring the morphological evolution in mixed-dimensional lead bromide perovskite films with lamellar-stacked perovskite nanoplatelets. *Nanoscale Horizons* **2019**, *4* (5), 1139−1144.

(154) Worku, M.; He, Q.; Xu, L. J.; Hong, J.; Yang, R. X.; Tan, L. Z.; Ma, B. Phase Control and In Situ Passivation of Quasi-2D Metal Halide Perovskites for Spectrally Stable Blue Light-Emitting Diodes. *ACS Appl. Mater. Interfaces* **2020**, *12* (40), 45056−45063.

(155) Tsai, H.; Nie, W.; Blancon, J.-C.; Stoumpos, C. C.; Soe, C. M. M.; Yoo, J.; Crochet, J.; Tretiak, S.; Even, J.; Sadhanala, A.; Azzellino, G.; Brenes, R.; Ajayan, P. M.; Bulović, V.; Stranks, S. D.; Friend, R. H.; Kanatzidis, M. G.; Mohite, A. D. Stable Light-Emitting Diodes Using Phase-Pure Ruddlesden−Popper Layered Perovskites. *Adv. Mater.* **2018**, *30* (6), 1704217.

(156) Hidalgo, J.; Perini, C. A. R.; Castro-Mendez, A. F.; Jones, D.; Kobler, H.; Lai, B.; Li, R. P.; Sun, S. J.; Abate, A.; Correa-Baena, J. P. Moisture-Induced Crystallographic Reorientations and Effects on Charge Carrier Extraction in Metal Halide Perovskite Solar Cells. *ACS Energy Lett.* **2020**, *5* (11), 3526−3534.

(157) Han, Y.; Wang, J.; Bischak, C. G.; Kim, S.; Lee, K.; Shin, D.; Lee, M. J.; Ginger, D. S.; Hwang, I. Significance of Ambient Temperature Control for Highly Reproducible Layered Perovskite Light-Emitting Diodes. *ACS Photonics* **2020**, *7* (9), 2489−2497.

(158) McMeekin, D. P.; Sadoughi, G.; Rehman, W.; Eperon, G. E.; Saliba, M.; Hörantner, M. T.; Haghighirad, A.; Sakai, N.; Korte, L.; Rech, B.; Johnston, M. B.; Herz, L. M.; Snaith, H. J. A mixed-cation lead mixed-halide perovskite absorber for tandem solar cells. *Science* **2016**, *351* (6269), 151.

(159) Pont, S.; Bryant, D.; Lin, C.-T.; Aristidou, N.; Wheeler, S.; Ma, X.; Godin, R.; Haque, S. A.; Durrant, J. R. Tuning CH3NH3Pb(I1−xBrx)3 perovskite oxygen stability in thin films and solar cells. *J. Mater. Chem. A* **2017**, *5* (20), 9553−9560.

(160) Aziz, A.; Aristidou, N.; Bu, X.; Westbrook, R. J. E.; Haque, S. A.; Islam, M. S. Understanding the Enhanced Stability of Bromide Substitution in Lead Iodide Perovskites. *Chem. Mater.* **2020**, *32* (1), 400−409.

(161) Quan, L. N.; García de Arquer, F. P.; Sabatini, R. P.; Sargent, E. H. Perovskites for Light Emission. *Adv. Mater.* **2018**, *30* (45), 1801996.

(162) Fang, H.-H.; Adjokatse, S.; Wei, H.; Yang, J.; Blake, G. R.; Huang, J.; Even, J.; Loi, M. A. Ultrahigh sensitivity of methylammonium lead tribromide perovskite single crystals to environmental gases. *Science Advances* **2016**, *2* (7), e1600534.

(163) Noh, J. H.; Im, S. H.; Heo, J. H.; Mandal, T. N.; Seok, S. I. Chemical Management for Colorful, Efficient, and Stable Inorganic−Organic Hybrid Nanostructured Solar Cells. *Nano Lett.* **2013**, *13* (4), 1764−1769.

(164) Misra, R. K.; Ciammaruchi, L.; Aharon, S.; Mogilyansky, D.; Etgar, L.; Visoly-Fisher, I.; Katz, E. A. Effect of Halide Composition on the Photochemical Stability of Perovskite Photovoltaic Materials. *ChemSusChem* **2016**, *9* (18), 2572−2577.

(165) Nagabhushana, G. P.; Shivaramaiah, R.; Navrotsky, A. Direct calorimetric verification of thermodynamic instability of lead halide hybrid perovskites. *Proc. Natl. Acad. Sci. U. S. A.* **2016**, *113* (28), 7717−7721.

(166) Lai, H.; Kan, B.; Liu, T.; Zheng, N.; Xie, Z.; Zhou, T.; Wan, X.; Zhang, X.; Liu, Y.; Chen, Y. Two-Dimensional Ruddlesden−Popper Perovskite with Nanorod-like Morphology for Solar Cells with Efficiency Exceeding 15%. *J. Am. Chem. Soc.* **2018**, *140* (37), 11639−11646.

(167) Gruverman, A.; Kholkin, A. Nanoscale ferroelectrics: processing, characterization and future trends. *Rep. Prog. Phys.* **2006**, *69* (8), 2443−2474.

(168) Liu, Y.; Zhang, Y.; Chow, M.-J.; Chen, Q. N.; Li, J. Biological Ferroelectricity Uncovered in Aortic Walls by Piezoresponse Force Microscopy. *Phys. Rev. Lett.* **2012**, *108* (7), 078103.

(169) Gruverman, A.; Alexe, M.; Meier, D. Piezoresponse force microscopy and nanoferroic phenomena. *Nat. Commun.* **2019**, *10* (1), 1661.

(170) Park, I.-H.; Zhang, Q.; Kwon, K. C.; Zhu, Z.; Yu, W.; Leng, K.; Giovanni, D.; Choi, H. S.; Abdelwahab, I.; Xu, Q.-H.; Sum, T. C.; Loh, K. P. Ferroelectricity and Rashba Effect in a Two-Dimensional

Dion-Jacobson Hybrid Organic–Inorganic Perovskite. *J. Am. Chem. Soc.* **2019**, *141* (40), 15972–15976.

(171) Sha, T.-T.; Xiong, Y.-A.; Pan, Q.; Chen, X.-G.; Song, X.-J.; Yao, J.; Miao, S.-R.; Jing, Z.-Y.; Feng, Z.-J.; You, Y.-M.; Xiong, R.-G. Fluorinated 2D Lead Iodide Perovskite Ferroelectrics. *Adv. Mater.* **2019**, *31* (30), 1901843.

(172) Shi, P.-P.; Tang, Y.-Y.; Li, P.-F.; Liao, W.-Q.; Wang, Z.-X.; Ye, Q.; Xiong, R.-G. Symmetry breaking in molecular ferroelectrics. *Chem. Soc. Rev.* **2016**, *45* (14), 3811–3827.